Petrological Evidence for Prominent Melt-Mush Reactions During Slow-Spreading Oceanic Accretion

Marine Boulanger, Marguerite Godard, Benoit Ildefonse, Malissa Bakouche

Geochemistry, Geophysics, Geosystems®

AGU ADVANCING EARTH AND SPACE SCIENCES

RESEARCH ARTICLE
10.1029/2023GC011409

Petrological Evidence for Prominent Melt-Mush Reactions During Slow-Spreading Oceanic Accretion

Marine Boulanger[1,2], Marguerite Godard[2], Benoit Ildefonse[2], and Malissa Bakouche[2,3]

[1]Université Clermont Auvergne, CNRS, IRD, OPGC, Laboratoire Magmas et Volcans, France, [2]Géosciences Montpellier, CNRS, Université de Montpellier, Montpellier, France, [3]Géosciences Environnement Toulouse (GET), CNRS UMR 5563 (CNRS/UPS/IRD/CNES), Université de Toulouse, Observatoire Midi-Pyrénées, Toulouse, France

Abstract The structure of the lithosphere and the associated magmatic systems found in different locations along slow-spreading ridges can vary dramatically, from melt-starved to magmatically robust segments. A growing number of studies suggest that the evolution of the magmatic crust being governed solely by fractional crystallization is too simplistic. Reactions between migrating melts and their surroundings play a key role during accretion, yet the full extent of their impact is still to be resolved. We present here the results of a petrological, microstructural, and in situ geochemical study of two drilled sequences from the Kane Megamullion and Atlantis Massif oceanic core complexes. We show that melt-mush reactions generate locally strong textural and/or geochemical heterogeneity at the cm-scale, but their impact can also be identified at the 100 m-scale. We found evidence for assimilation at various degrees of primitive lithologies of potential mantle origin within the gabbroic sequence at both locations, in addition to typical melt-mush reactions previously described in other slow-spread magmatic systems. Observations and numerical modeling confirm the similarity of the reactions impacting both sequences. However, the regime of the reactions (ranges of assimilation to crystallization ratios) seems to vary between Kane Megamullion and Atlantis Massif, variations which likely result from differences in melt fractions present during melt-mush reactions. We infer relying on our observations and previous studies that the regime of the reactions is most likely controlled by the melt flux during the formation of the two sections.

Key Points:

- Kane Megamullion and Atlantis Massif oceanic core complexes record widespread melt-mush reactions at different scales
- In addition to typical melt-mush reactions, assimilation of primitive (mantle?) lithologies is observed within gabbro sequences
- Discrepancies in the melt-mush reaction signatures of the two sequences reveal variable melt dynamics during accretion

Supporting Information:

Supporting Information may be found in the online version of this article.

Correspondence to:

M. Boulanger,
marine.boulanger@uca.fr

Citation:

Boulanger, M., Godard, M., Ildefonse, B., & Bakouche, M. (2024). Petrological evidence for prominent melt-mush reactions during slow-spreading oceanic accretion. *Geochemistry, Geophysics, Geosystems*, *25*, e2023GC011409. https://doi.org/10.1029/2023GC011409

Received 20 DEC 2023
Accepted 10 JUL 2024

Author Contributions:

Conceptualization: Marine Boulanger
Data curation: Marine Boulanger, Malissa Bakouche
Formal analysis: Marine Boulanger, Marguerite Godard
Funding acquisition: Marine Boulanger, Marguerite Godard, Benoit Ildefonse
Investigation: Marine Boulanger, Malissa Bakouche
Methodology: Marine Boulanger
Project administration: Marine Boulanger, Benoit Ildefonse
Resources: Marine Boulanger, Benoit Ildefonse

1. Introduction

Both magmatic accretion and tectonic displacement accommodate extension at slow-spreading ridges (Buck et al., 2005). The prevalence of one of the two processes depends on the rate of magma supply below the ridge that strongly varies along-axis (Cannat et al., 2019). Magmatic accretion at slow-spreading ridges involves repetitive melt intrusions within mantle-derived lithosphere and/or preexisting magma bodies at various degrees of crystallization (Boulanger et al., 2021; Canales et al., 2017; Drouin et al., 2010; Godard et al., 2009; Grimes et al., 2008; Sanfilippo & Tribuzio, 2013). The resulting crust is characterized by a strong heterogeneity at all scales, with depth and along the mid-oceanic ridge system (Cannat et al., 1997; Carbotte et al., 2016; Dick, MacLeod, et al., 2019; Escartín et al., 2008; Smith et al., 2012). Active magma reservoirs consist mainly of crystal mush behaving as open systems, subject to regular melt injections and internal melt migration (Boulanger et al., 2020; Cordier et al., 2010). Such conditions likely favor processes of interactions between migrating melts and their surroundings (Boulanger & France, 2023; Coogan et al., 2000; Drouin et al., 2009; Ferrando et al., 2018; Gardner et al., 2020; Lissenberg et al., 2019), a concept previously developed for mantle lithologies (Bodinier et al., 1990; Kelemen et al., 1992). These interactions have been given different names in the literature, including melt-rock reactions, reactive melt percolation or (porous) flow, melt-mush reactions, or partial melting (e.g., Leuthold et al., 2018; Lissenberg & Dick, 2008; Mathez, 1995; Yang et al., 2019; Zhang & Liu, 2023), but they all can be described as a two stages magmatic process. One stage is the assimilation of a preexisting material, usually described as a mineral assemblage, by a melt from which new minerals crystallize. The other stage is crystallization, which produces minerals that can record characteristic geochemical signatures. The mineralogy of the dissolving and crystallizing phases are not always similar (Basch et al., 2022; Boulanger et al., 2020, 2021; Ferrando et al., 2018; Ferrando, France, et al., 2021; Lissenberg & Dick, 2008; Lissenberg & MacLeod, 2016; Sanfilippo et al., 2020; Zhang et al., 2020). In addition, the assimilation and crystallization stages are not necessarily synchronous, as suggested by the discrepancy between the reactions identified in the gabbroic archive and the reactions modeled thermodynamically (Boulanger & France, 2023). The total amount of preexisting

Software: Benoit Ildefonse
Supervision: Marine Boulanger
Validation: Marine Boulanger, Marguerite Godard, Benoit Ildefonse, Malissa Bakouche
Visualization: Marine Boulanger
Writing – original draft: Marine Boulanger
Writing – review & editing: Marguerite Godard, Benoit Ildefonse, Malissa Bakouche

material affected by the reactions is difficult to reconstruct from the cumulate record, yet the process has the potential to substantially affect the chemistry of the melts and the mineralogy of the solid residue.

A growing amount of evidence indicates the prevalence of these interactions, called hereafter melt-mush reactions, in the formation of oceanic cumulates (Boulanger & France, 2023; Lissenberg et al., 2019, and references therein) and their possible contribution to mid-ocean ridge basalt (MORB) geochemical signatures (Danyushevsky et al., 2003; Laubier et al., 2012; Lissenberg & Dick, 2008; Shimizu et al., 2019). Characteristic cumulate disequilibrium textures are visible for minerals subject to assimilation, mostly olivine (Ol) and/or plagioclase (Pl). Concomitant crystallization leads to the formation of minerals with poikilitic textures or highly interstitial textures, mostly clinopyroxene (Cpx) and to a lesser extent Pl. The chemistry of the systems also provides clues to the occurrence and characteristics of melt-mush reactions. For MORBs, interactions with lower oceanic crust are assumed to generate melts with lower Ca and higher Mg or higher Al contents, for example, due to Ol or Pl assimilation (Ferrando et al., 2018; Laubier et al., 2012; Lissenberg & Dick, 2008; Paquet et al., 2016). Mineral rare earth elements (REE) content in oceanic cumulates also deviates towards higher fractionation and enrichment compared to the chemical trends expected after crystallization only (Basch et al., 2022; Boulanger et al., 2020, 2021; Coogan et al., 2000; Ferrando, France, et al., 2021; Lissenberg & MacLeod, 2016; Zhang et al., 2020).

Significant progress on the impact of melt-mush reactions on differentiation with depth reconstructed with magmatic structures was made at Atlantis Bank (Southwest Indian Ridge), thanks to the two gabbroic sequences drilled there (Dick et al., 1999; Dick, MacLeod, et al., 2019; MacLeod et al., 2017). Melt migration by intrusion and by percolation are both at play during the formation of plutonic sequences (Bloomer et al., 1991; Boulanger et al., 2021; Ferrando, France, et al., 2021). Percolation, where present, controls the structure of the magmatic sequences and the texture and geochemistry of the gabbroic rocks. Evidence of melt-mush reactions is widespread, from the most primitive (troctolites of ODP Hole 735B, Boulanger et al., 2020; Zhang et al., 2020, 2021) to the most evolved lithologies (oxide gabbros of IODP Hole U1473A, Ferrando et al., 2022; Gardner et al., 2020, 2023; Zhang et al., 2020). Melt-mush reactions seem to be strongly involved in the formation of magma reservoirs (Boulanger et al., 2020) and, overall, in the formation of large-scale intrusive units (Dick, Kvassnes, et al., 2019; Dick, MacLeod, et al., 2019; Ferrando, France, et al., 2021; Zhang & Liu, 2023) that represent, to some extent, percolation columns. The possibility of melts carrying melt-mush reaction signatures (called hereafter reactive melts) reaching the surface is also high. For instance, at Atlantis Bank, reaction-derived slightly to highly evolved MORB conduits crosscutting the gabbroic sequences were described by Sanfilippo et al. (2020) and Zhang et al. (2021). In addition, pockets of reactive melts collected from surrounding coarse-grained gabbro mushes are widespread and occur as fine-grained heterogeneities (Ferrando, France, et al., 2021). This opens the possibility for large-scale accumulation and migration of reactive melts through the gabbroic sequences forming the Atlantis Bank oceanic core complex (OCC).

The occurrence of melt-mush reactions is recognized at different scales, from individual samples to that of crustal sequences and at different locations in ophiolites and crustal sequences drilled at mid-ocean ridges. However, the impact of melt-mush reactions on oceanic crust accretion is to be better defined in locations other than Atlantis Bank. Melt-mush reactions implication in the formation of the highly heterogeneous magmatic sequences generated at MOR is also still pending. Here, we investigate two gabbroic sequences from the well-described Atlantis Massif (AM; Blackman et al., 2011; Godard et al., 2009) and Kane Megamullion (KM; Cannat et al., 1997) OCCs. Based on their current description, these two sequences have the potential to contain a large amount of information on the processes involved in magmatic accretion, where melt-mush reactions could play a role (Coogan et al., 2000; Drouin et al., 2009, 2010; Ferrando et al., 2018). This comparative study of the 70 m-long ODP Hole 923A (Cannat, Karson, & Miller, 1995) and a 400 m-long section from IODP Hole U1309D (Blackman et al., 2006) allows us to study in detail two magmatic systems and accretion processes at two different scales along the Mid-Atlantic Ridge (MAR).

2. Geological Settings

2.1. Atlantis Massif

Atlantis Massif is an OCC located on the western flank of the Atlantis Fracture Zone at 30°N along the MAR (Figure 1a). The ∼15 km long and ∼10 km wide structure formed during the last ∼2 My. The half-spreading rate of the ridge axis at this location is 12 mm/y. The surface of the dome structure is characterized by a well-

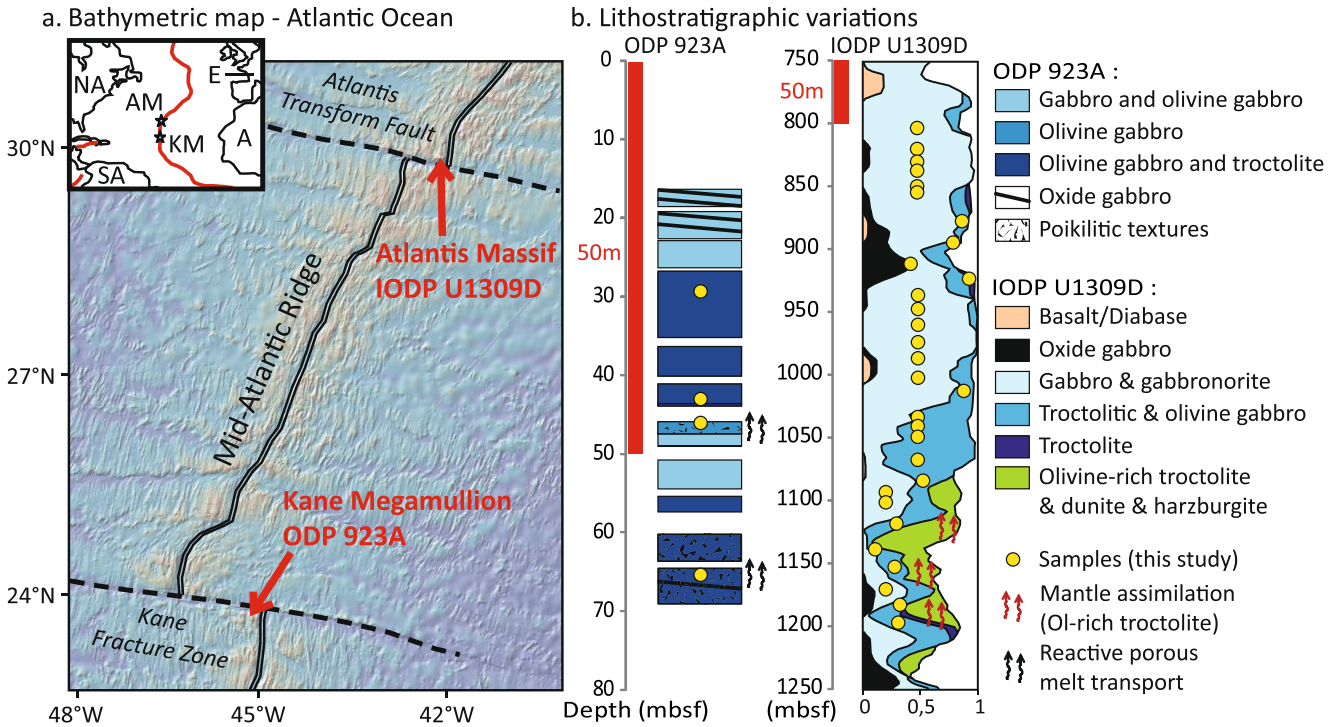

Figure 1. (a) 3D bathymetric map of the Mid-Atlantic Ridge between 23° and 31°N. Bathymetry map generated with GeoMapApp (https://www.geomapapp.org) using the GMRT grid (Ryan et al., 2009). Doubled lines: MOR, dashed lines: fracture zones, NA: North America, SA: South America, AM: Atlantis Massif, KM: Kane Megamullion, E: Europe, A: Africa. (b) Lithostratigraphic variations of the studied sections from ODP Hole 923A (based on Cannat, Karson, and Miller (1995)) and from IODP Hole U1309D (recovery and fraction of cores interval from Blackman et al. (2006)). The depth and lithology of the samples are indicated by the yellow points on the lithostratigraphic columns. "Mantle assimilation" from Drouin et al. (2009, 2010), Ferrando et al. (2018), Suhr et al. (2008), and "reactive porous melt transport" from Coogan et al. (2000).

defined corrugated surface that represents the preserved footwall of the detachment fault (Blackman et al., 2004; Cann et al., 1997). Gravity anomalies indicate the presence of ultramafic rocks and an uneven distribution of gabbroic crustal lithologies within the structure (Blackman et al., 2009; Canales et al., 2008; Nooner et al., 2003). IODP Hole U1309D drilled during Exp. 304/305 reaches 1,415 mbsf (meters below sea floor) and recovered a total of 1,043 m of cores, and has been deepened by 83 m during Exp. 399 (for a total depth of 1,498 mbsf). The most abundant lithology is gabbro (including gabbronorites, 55.7%) followed by Ol gabbro (25.5%) and gabbros with oxides (7%). About 8% of Ol-rich lithologies (troctolites and Ol-rich troctolites) in addition to ∼0.3% ultramafic rocks described as peridotites were also recovered (Blackman et al., 2006). Gabbros are intrusive within Ol-rich lithologies, with sharp intrusive contacts above ∼650 mbsf and more diffuse contacts deeper in the section. Ol gabbros locally grade to troctolite, and gabbros with oxides are present in the form of patches dispersed within typically undeformed coarse-grained gabbro. Oxide gabbros sometimes occur as dikelets or layers within other rock types and are associated with ductile deformation (Blackman et al., 2006). Godard et al. (2009) deduced from the strong lithological variations lacking downhole systematic associated with intrusive contacts that the section is built of a series of cross-cutting magmatic units. Detailed studies of the olivine-rich lithologies by Drouin et al. (2009, 2010) and Ferrando et al. (2018) described the process of local assimilation of lithologies originating from the mantle by intrusive melts during periods of sustained magmatic activity at depth. Another study focused on one of these areas of mantle assimilation together with the overlying ∼300 m-long gabbroic unit (Suhr et al., 2008). This overlying unit is a rather homogeneous gabbro sequence compared to the rest of the drilled cores and was described as a magmatic differentiation unit, yet details of its formation remain undetermined. For this study, we focused on the gabbroic lithologies (sensu lato, excluding olivine-rich lithologies, peridotites, and oxide gabbros) located between 800 and 1,200 mbsf, that is, between the top of the magmatic differentiation unit and the base of the mantle assimilation area.

2.2. Kane Megamullion

Kane Megamullion is constituted by a series of domes located ∼35 km west of the junction between the Kane fracture zone and the MAR at 23°30′N (Figure 1a, Dick et al., 2008). The complex represents the footwall of a long-lived detachment fault exposing both (altered) peridotites and gabbro bodies, likely formed during a period of limited magmatic accretion (Cannat et al., 1997). Five different drilling sites located in the footwall of the detachment allowed the recovery of gabbroic lithologies, mainly interlayered troctolite and olivine gabbro (Sites 921–924, Cannat, Karson, Miller, & Party, 1995). ODP Hole 923A is the deepest drilled in the gabbroic sequences, with a recovery rate of ∼75% over the total 70 m drilled below the seafloor (Cannat, Karson, & Miller, 1995). In detail, the main lithologies are olivine gabbro, gabbro, poikilitic gabbro, and troctolite. Both textures and modes vary on scales of cm to meters (Figure 7c), and present locally well-defined layering. Compared to the other sites, alteration is limited in ODP Hole 923A, which contains also less oxide gabbro and gabbronorite. Lissenberg and Dick (2008) identified in dredge gabbros from the KM area evidence for melt-rock reactions or melt-mush reactions in both the textures of the samples (e.g., resorbed plagioclase oikocryst in high-Mg clinopyroxene) and their composition (high-Mg clinopyroxenes that crystallized the latest in the samples, minor element compositions in disequilibrium with MORB melts). Similar conclusions were reached by Coogan et al. (2000) in their study of the poikilitic gabbros from ODP Hole 923A. Ross and Elthon (1997) had previously studied these gabbros and inferred the occurrence of postcumulus processes, and crystallization of clinopyroxene "from evolving intercumulus melts buffered at high Mg# by interaction with cumulus crystals." Although this hypothesis involves partial equilibration with trapped melts, Coogan et al. (2000) advocated for reactive porous melt migration through the crystal mush "reacting and partially reequilibrating with the crystal assemblage," relying on samples from Hole 923A.

3. Samples and Methods

3.1. Sample Selection

Two sections were targeted relying on previous descriptions from drilling campaigns and post-cruise research. The sampling strategy was adjusted during the redescription of the sections at the Bremen Core Repository (Germany). The full sample list is available in Table S1 of Supporting Information S1, with mineral modes determined by using the ImageJ software on thin section scans (Schneider et al., 2012) for Hole U1309D and relying on the EBSD data for Hole 923A. The 400 m-long section from IODP Hole U1309D (AM) was sampled to collect representative gabbroic lithologies at regular intervals (every 13 m on average, Figure 1b). Samples were collected from the top of the "differentiation" unit at ∼800 mbsf (Suhr et al., 2008) down to the lowest part of the olivine-rich interval Zone 4 (Drouin et al., 2009, 2010). We studied the most abundant gabbroic lithologies previously described as gabbronorite, gabbro, olivine gabbro and troctolite, deliberately avoiding the olivine-rich and ultramafic intervals of potential mantle origin (Drouin et al., 2009, 2010; Ferrando et al., 2018, 2020) and the suspected more complex and late oxide gabbro intervals. The collected samples all classify as olivine gabbros and gabbros (0%–46% Ol, 26%–62% Pl, and 20%–64% Cpx). The sampling of the 70 m long section from ODP Hole 923A (KM) targeted specific igneous structures at depth in three main areas (Figure 1b, Cannat, Karson, & Miller, 1995): a well-defined modal and grain size layering located at ∼30 mbsf, a (non-recovered) contact between gabbros and troctolitic gabbros between ∼40 and 50 mbsf, and variations of mode and texture with irregular and diffuse contacts between olivine gabbros and troctolites at ∼65 mbsf. A total of 10 samples were collected from OPD Hole 923A and 31 samples for IODP Hole U1309D. Only samples devoid of strong crystal-plastic deformation and alteration were selected to focus on primary magmatic features.

3.2. EBSD and Chemical Maps

Crystallographic orientations were measured, and chemical maps were acquired for the eleven thin sections prepared from the ten ODP Hole 923A samples, by Electron BackScattered Diffraction (EBSD) and by Energy Dispersive Spectrometry (EDS), respectively, at Géosciences Montpellier (France). We used the Field Emission Gun CamScan X500FE Crystal Probe SEM facility equipped with the Oxford instrument Nordlys® EBSD detector and EDS X-MaxN 20 mm^2 detectors, and the AZtecHKL (Oxford) software. Acquisition of the diffraction patterns was conducted at 20 kV acceleration voltage and controlled vacuum at 2 Pa. The measurement step size varied between 12 and 25 μm to detect interstitial mineral and potential chemical variations by EDS. The pre-data processing indexation rate was 95.2% on average, excluding the thin section presenting the strongest alteration

(olivine altered in non-indexed serpentine) with an indexation rate of 72.7%. Indexed minerals are plagioclase (Pl), olivine (Ol), clinopyroxene (Cpx), orthopyroxene (Opx), amphibole (Amp), magnetite (Mt), ilmenite (Ilm), and troilite (Tr) for sulfide phases.

Post-acquisition data processing was performed using the Channel 5 (Oxford) software suite and the MTEX free toolbox for Matlab (Mainprice et al., 2014). The first step of data treatment consists of the automatic removal of isolated pixels surrounded by pixels indexed for another phase, and filling of the non-indexed pixels having at least 5 neighbors with the same orientation. The second step of data processing with MTEX allowed the calculation of grain boundaries based on a threshold value of 10° between adjacent pixels of the same phase, and the removal of small grains with an average diameter smaller than 5 pixels. In the case of twinned Pl, grain boundaries with boundary angles >175°, a rotation in (010) and (001) and around [010] and [001] were removed. The reconstructed Pl grain orientation was taken as the one of the largest twin domain identified, following the procedure developed by Allard et al. (2021). Additional grain and textural analyses together with Crystallographic Preferred Orientation (CPO) analysis were also performed using MTEX. Three of the maps were reoriented (by simple rotation) so that their geographic reference system corresponds to that of the drilled hole. Each parameter describing the fabric of the samples is detailed in Table S2 of Supporting Information S1.

Intragrain misorientation is quantified as the angle between the crystallographic orientation of a particular pixel within a grain and the average orientation of all pixels of the same grain (Mis2Mean parameter). Here we use the average of the Mis2Mean parameter that is the grain orientation spread (GOS). The average GOS quantifies the grain misorientation per sample. The fabric strength and distribution density of the main crystallographic axes are determined by calculating the J index (e.g., Mainprice & Silver, 1993) of the orientation distribution function; J varies from 1 for a random distribution to infinity for a single perfectly uniform crystal. The symmetry of the mineral CPOs is evaluated by calculating the BA (for Pl) and BC indexes (for Ol and Cpx - Mainprice et al., 2014; Satsukawa et al., 2013). The BA and BC indexes are based on three other indexes P, G, and R (Point, Girdle and Random). The three indexes are calculated using the eigenvalues of the orientation tensor that represent the distribution of the crystallographic axes (or poles to crystallographic planes) in each pole figure (Satsukawa et al., 2013). BA and BC indexes vary between 0 and 1, and represent the relative weight of the fabrics defined by (100) and (010) for the former, and (010) and (001) for the latter, and thus the predominance of lineation with high BA and BC or foliation with low BA and BC (see Table S2 in Supporting Information S1).

3.3. Electron Probe Micro Analyzer (EPMA)

The major element concentrations of constitutive minerals of the eleven thin sections from ODP Hole 923A and fourteen samples from IODP Hole U1309D were quantified using EPMA at Géosciences Montpellier (France) with a Cameca SX100 equipped with 5 wavelength-dispersive X-ray spectrometers (WDS). Analyses were performed using 15 kV accelerating potential, 15 nA beam current and a focused beam. Counting times were 10 or 20 s depending on the element considered. Details on the counting times, considered mineral standards and errors are given in Table S3.

3.4. LA-ICP-MS

Trace element compositions of Ol (Figure S2 in Supporting Information S1), Pl (Figure S3 in Supporting Information S1) and Cpx (Figure S4 in Supporting Information S1) were determined using a ThermoFinnigan Element2 XR inductively coupled plasma mass spectrometer (eXtended Range ICP-MS) coupled with a laser ablation system Téledyne G2 (AETE-ISO facility, OSU OREME, Université de Montpellier). Signal acquisition was done in Time Resolved Acquisition, counting 120 s for background and 60 s for sample measurement. The frequency of the laser was of 10 Hz with an energy density of 6 J.cm^2 and a spot size of 110 µm for Ol and Pl. For Cpx, the frequency was of 8 Hz and the spot size of 65 µm. All ablation experiments were conducted under helium mixed with argon before entering the plasma. Data were processed with the GLITTER software. All concentrations were calibrated using the synthetic rhyolitic glass NIST 612 (reference values of Pearce et al., 1997). 43Ca was used as the internal standard for Cpx and 29Si for Ol and Pl, relative to the Ca and Si concentrations acquired by EPMA on the same minerals and, wherever possible, at the same location. The accuracy and repeatability of analyses were assessed using standard reference basalt BIR-1G (Table S4).

4. Results

4.1. Structure and Petrographic Variations

4.1.1. IODP Hole U1309D

Thirty one samples were collected from the bottom of the Ol-rich troctolite zone 4 (1,195 mbsf) up to the top of the "differentiation" unit at 805 mbsf (Suhr et al., 2008). The top ~300 m of the magmatic sequence (805–1,100 mbsf) is mostly composed of gabbronorite and gabbro to progressively more primitive Ol gabbro downward (Figure 1b, Blackman et al., 2006). Some diabase and oxide gabbro intervals are also present, the latter being the most altered lithology of the sequence (not sampled here). Below, gabbros and Ol gabbros alternate with troctolite and dunite. About 30% of the collected samples are gabbros, two of them bearing small amounts of oxides (<1%), ~60% are Ol gabbros and 10% are Ol-bearing gabbros (Figure 7c). Only one troctolite is found in sharp contact with an Ol gabbro in sample 305-U1309D-175R-2, 122–126 cm (see ODP/IODP sample nomenclature in Text S1). The grain size ranges from fine to very coarse-grained (average 0.4 cm), and a few crystals (mostly Cpx) are almost pegmatitic. About 50% of the samples present grain size variations, two of them with a sharp contact between a finer grained and a coarse-grained domain (305-U1309D-194R-2, 16–20 cm and 305-U1309D-202R-2, 85–89 cm). No clear intrusive contact was identified on the thin sections. Textures are highly variable between samples and sometimes within a single thin section. No systematics between the type of lithology and the sample texture has been identified except for the Ol-rich lithology as described thereafter. In addition to the three main minerals (Ol, Pl and in Cpx), Opx is present but the fraction is too low (<5%) to identify the samples as gabbronorites. Opx occurs as rims mainly around Mg-Fe minerals and as anhedral minerals. Rare spinel (mostly present in the troctolitic gabbro samples) and other accessory minerals are present (Amp and sulfides).

Olivines are fine to very coarse grained (>2 cm elongated minerals in Ol gabbro 305-U1309D-189R-4, 45–49 cm). They show rounded to angular shapes, and are present both as single crystals and aggregates depending on the sample considered (Figures 2b and 2c). The largest crystals present subgrain boundaries and a few kink bands. The alteration of Ol in serpentine is substantial in some of the Ol gabbros. Olivine chadacrysts are present in Pl and most Cpx (Figures 2a, 2e, and 2g); they often show irregular contacts with surrounding minerals (Figures 2b and 2c). Rare Pl chadacrysts are found in Ol (Figure 3a). Two Ol gabbros (305-U1309D-228R-4, 43–46 cm and 305-U1309D-232R-3, 3–7 cm) have textures similar to the Ol-rich troctolites described in the literature (Drouin et al., 2010; Ferrando et al., 2018): they present high concentrations of rounded Ol minerals embedded in large Cpx and Pl poikiloblasts (Figures 3a–3c). These samples are referred to as Ol-rich samples.

Plagioclases are fine to very coarse-grained, anhedral to rarely subhedral. Their morphology can drastically change from one sample to the other and within a single thin section. Gabbros (sensu lato) show irregular anhedral cumulus grains except for one Ol-bearing gabbro (305-U1309D-243R-2, 23–27 cm) that presents mostly Pl laths in very coarse grained Cpx oikocrysts. Both magmatic and deformation twins are visible (e.g., Figure 2b). Most grains show irregular grain boundaries (wavy) that crosscut the minerals at an angle to the main crystal axis and lengthwise (resorbed twins in several points along the main axis, Figures 2d, 2e, and 2h). Zoning is visible in polarized light but not ubiquitous in every grain of a single sample and is usually complex (resorbed zoning and irregular overgrowth, Figures 2b and 2f). Plagioclase chadacrysts are found in Ol but mostly Cpx grains, and occasionally show highly irregular grain boundaries (Figures 2d and 2h). Some coarse-grained Pl present rounded Ol chadacrysts, and rarely Cpx chadacrysts.

Clinopyroxenes are fine to very coarse grained, up to pegmatitic in some samples (e.g., gabbro 305-U1309D-168R-2, 25–29 cm and Ol gabbro 305-U1309D-228R-4, 43–46 cm). They are subhedral with massive shapes to poikilitic, and locally interstitial (Ol-rich samples). The pegmatitic grains (>30 mm, IODP conventions) found in the Ol-rich samples embed numerous rounded Ol and irregularly shaped Pl grains. Chadacryst distribution is heterogeneous: some areas present only Ol, others only Pl or a mix between the two, whilst Cpx cores are completely devoid of chadacrysts (Figures 2g and 3a). In some samples, Cpx grains contain areas filled with Opx and/or Amp exsolutions (Figure 2g). Cpx grains often present characteristic intergrowths (Figure 2i) and some twins. They show irregular grain boundaries and no visible zoning in polarized light. In the upper part of the section, some grains can be described as zoned in the amount of chadacrysts they contain. They present more chadacrysts in their rims, with more resorbed grain boundaries and/or smaller grains (Figure 2g).

10.1029/2023GC011409

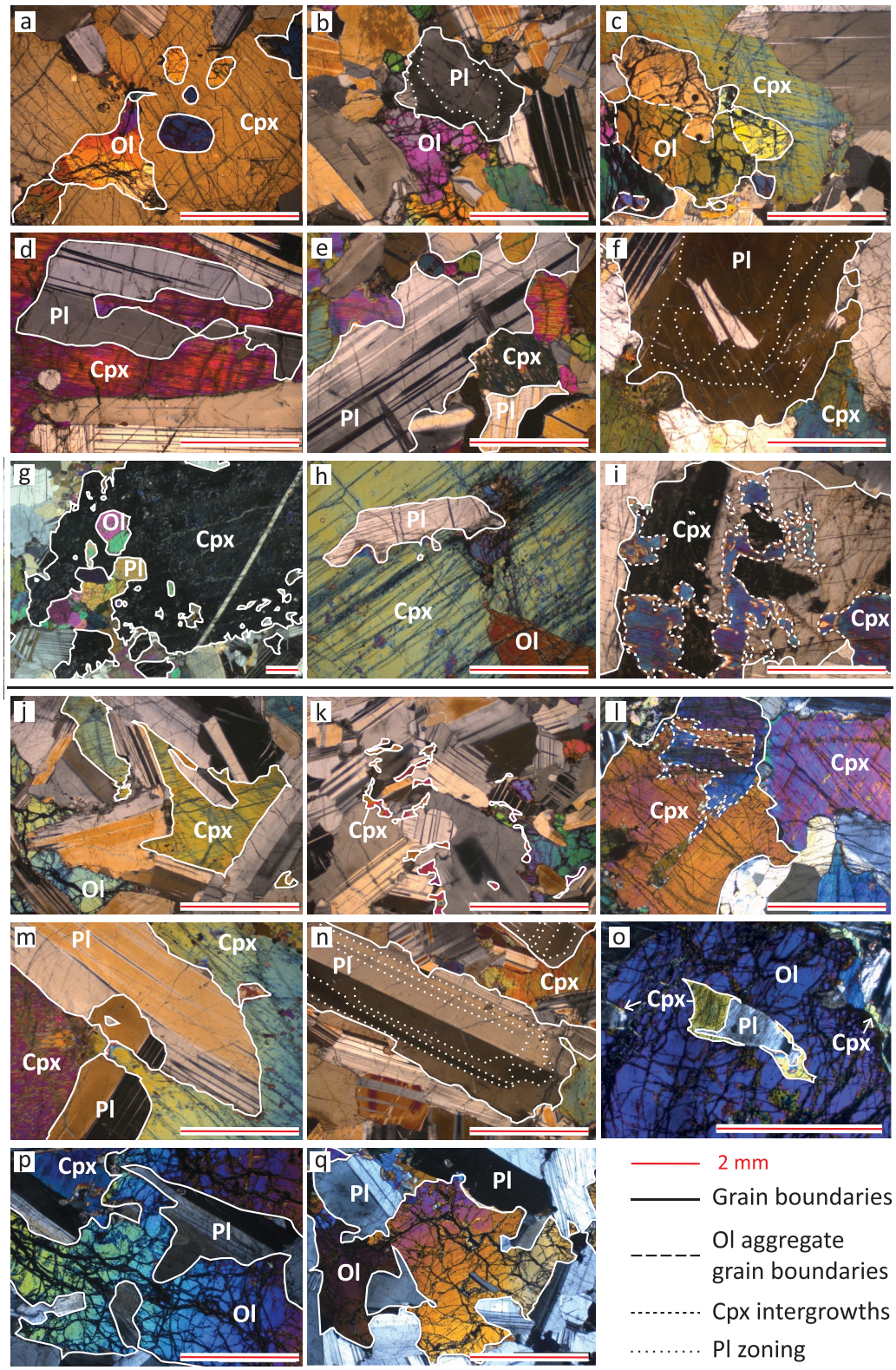

Figure 2.

4.1.2. ODP Hole 923A

Ten samples were collected at three different depths along ODP Hole 923A (Figure 1). Specific igneous structures were targeted and are detailed in the following (see Table S1 in Supporting Information S1).

The top unit located at 29 mbsf presents modal and grain size layering between Ol gabbros and troctolites as previously described by Cannat, Karson, and Miller (1995). The contacts are inclined and marked by the appearance/disappearance of Cpx and grain size variations. Four thin sections were made from the three samples collected at ∼30 mbsf and sample five different lithologies. Layer 1 is a fine-grained Ol gabbro in gradational contact with layer 2 (sample 153-923A-8R-1, 31–34 cm). Layer 2 is also an Ol gabbro (more troctolitic than layer 1) in gradational contact with an Ol-bearing gabbro band (layer 3, sample 153-923A-8R-1, 40–47 cm). In the same sample the contact with layer 4 troctolite is sharp on both sides. The textures of the four top layers are similar. Olivines are fine to medium grained and angular in shape. Some of the Ol aggregates or single crystals present small Pl chadacrysts, and do not present clear resorption features. Euhedral Pl are fine- to medium-grained; they show mainly deformation twins and the coarser grains present clear complex zoning (Figures 2k, 2m, and 2p). Clinopyroxenes are fine-grained and interstitial in the Ol-Pl matrix, even in the Ol-bearing gabbro layer 3 (Figure 2k). The deepest layer 5 is a coarse-grained Ol gabbro (153-923A-8R-1, 60–63 cm). Olivines are medium- to coarse-grained, angular in shape, and present well-developed kink bands in the coarser grains. Plagioclases are medium to coarse-grained, euhedral to subhedral. They also present complex zoning and more developed deformation twins compared to the top layers. Plagioclase chadacrysts are found in coarse-grained Cpx. All Pl show irregular contacts with surrounding minerals. Clinopyroxenes are anhedral and rounded, and present areas with Opx and Amph exsolutions (Figures 2l and 2m). About 1% oxides (rounded interstitial pockets) are found in layer 5.

The middle unit has been described as a composite of gabbro, Ol gabbro and troctolite. The sampled area between 42 and 46 mbsf targets the three main lithologies of Unit 3. There is one cataclastic interval between the top sample and the two lowest samples. The top sample (153-923A-11R-2, 74–76 cm) is a deformed Ol gabbro that shows Pl recrystallization at grain boundaries and fractures crosscutting the sample. Olivines are present as a fine-grained aggregate, one coarse-grained euhedral grain and one fine-grained rounded Olivine chadacryst in a large Cpx. Plagioclases are euhedral, and either fine-grained (recrystallized) or coarse-grained with well-developed deformation twins. Some of the coarse Pl show complex zoning. Euhedral coarse-grained Cpx are fractured, and present domains with Opx exsolution and Amp previously described as resulting from a near-solidus reaction with an evolved hydrous silicate melt (Coogan et al., 2001). The second sample is an altered troctolitic gabbro with Ol-rich textures (153-923A-12R-1, 74–77 cm, Figure 3d). It contains rounded Ol chadacrysts embedded in pegmatitic Cpx in the top half or smaller Pl oikocrysts in the bottom half of the sample (Figure 3e). Olivine shapes are more irregular than the grains described in the Ol-rich sample of Hole U1309D with almost skeletal-shaped resorbed grains. Rounded fine-grained Ol are mostly present in Pl oikocrysts, and medium- to coarse-grained Ol with more complex shapes are found within Cpx oikocrysts (Figure 3f). Plagioclases are anhedral, and show magmatic or deformation twins. Either plagioclase grains embed small Ol chadacrysts or they are present as small rounded chadacrysts with magmatic twins in the pegmatitic Cpx. Cpx are present as two pegmatitic oikocrysts in the top half, and small interstitial grains in the bottom half of the sample (Figures 3f and 4d). The third sample (153-923A-12R-1, 118–121 cm) is a troctolite containing one pegmatitic Ol grain and a few rounded irregularly shaped medium-grained Ol (Figures 4e and 4f). The pegmatitic Ol presents a lobated morphology with rounded

Figure 2. Microphotographs (cross-polarized light) of samples from IODP Hole U1309D (a–i) and ODP Hole 923A (j–q) presenting reaction textures. (a) Rounded Ol chadacrysts in a coarse grained Cpx. Ol gabbro 305-U1309D-175R-2W, 122–126 cm. (b) Pl grain presenting complex zoning and irregular grain boundaries. Ol gabbro 305-U1309D-208R-3W, 52–56 cm. (c) Ol aggregate with wavy grain boundaries with adjacent Cpx and resorbed structures at contact with Pl. Ol gabbro 305-U1309D-236R-3W, 17–21 cm. (d) Heavily resorbed Pl grain within a poikilitic Cpx grain. Gabbro 305-U1309D-168R-2W, 25–29 cm. (e) Pl grain with irregular grain boundaries enclosing small, rounded Ol grains. Ol gabbro 305-U1309D-174R-3W, 26–30 cm. (f) Large Pl grain with complex zoning and irregular grain boundaries. Ol-bearing gabbro 305-U1309D-184R-1W, 23–27 cm. (g) Poikilitic coarse grained Cpx with exsolutions and no chadacryst at its core and a large amount of small resorbed chadacrysts of Ol and Pl towards the rim of the grain, and (h) Resorbed Pl chadacryst within a poikilitic coarse grained Cpx. Troctolite 153-923A-8R-1W, 31–34 cm. (i) Cpx intergrowths. Gabbro 305-U1309D-225R-2W, 87–90 cm. (j) Interstitial Cpx from a "poikilitic gabbro" (Cannat, Karson, & Miller, 1995). Ol gabbro 153-923A-16R-1W, 52–55 cm. (k) Small interstitial Cpx from the top unit (layer 1). Troctolite 153-923A-8R-1W, 31–34 cm. (l) Cpx intergrowths and (m) resorbed Pl laths trapped within coarse grained Cpx. Ol gabbro 153-923A-8R-1W, 60–63 cm. (n) Pl grains with complex zoning and irregular grain boundaries. Ol-bearing gabbro 153-923A-16R-1W, 89–91 cm. (o) Pegmatitic Ol grain with a resorbed Pl "chadacryst," and interstitial Cpx present at the contact between the Ol and surrounding grains. Troctolite 153-923A-12R-1W, 118–121 cm. (p and q) Sub-poikilitic Ol grains partially enclosing Pl grains. Troctolite 153-923A-8R-1W, 40–47 cm. Figure available without any grain boundaries or zoning highlights in Figure S6 of Supporting Information S1.

10.1029/2023GC011409

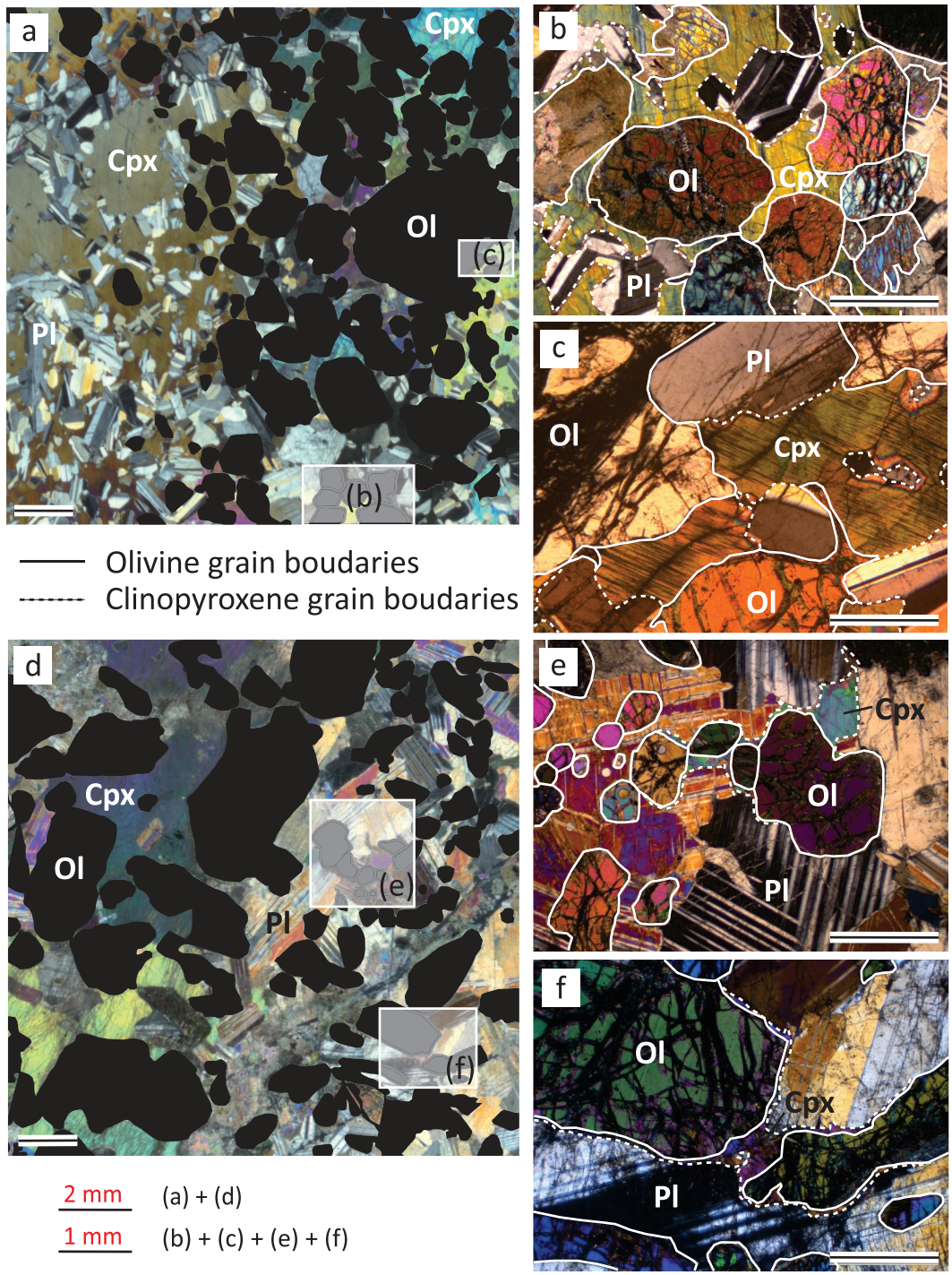

Figure 3. Microphotographs (cross-polarized light) of characteristic textures of olivine-rich type samples from IODP Hole U1309D (a–c, sample 305-U1309D-228R-4W, 43–46 cm) and ODP Hole 923A (d–f, sample 153-923A-12R-1W, 74–77 cm). This last section is thicker than 30 µm, hence shifting the coloring of some Pl to the end of the first order, and some Ol to the third order. (a) High concentrations of Pl (lower left) and Ol (upper right) chadacrysts within pegmatitic poikilitic Cpx grains. (b) Heavily rounded Ol grains with locally irregular grain boundaries enclosed within a single Cpx crystal. (c) Contact between a large Ol grain and surrounding Pl and interstitial Cpx. Note the morphology of the bottom Ol presenting interstitial branching. (d) Ol chadacrysts with rounded grains boundaries within pegmatitic Cpx (left) and coarse-grained Pl oikocrysts (right). (e) Fine-grained heavily rounded Ol grains within poikilitic Pl grains. Note the interstitial Cpx coating the contact between Ol and Pl. (f) Interstitial Cpx between Pl and Ol grains presenting resorption features. Figure available without any grain boundaries or zoning highlights in Figure S7 of Supporting Information S1.

10.1029/2023GC011409

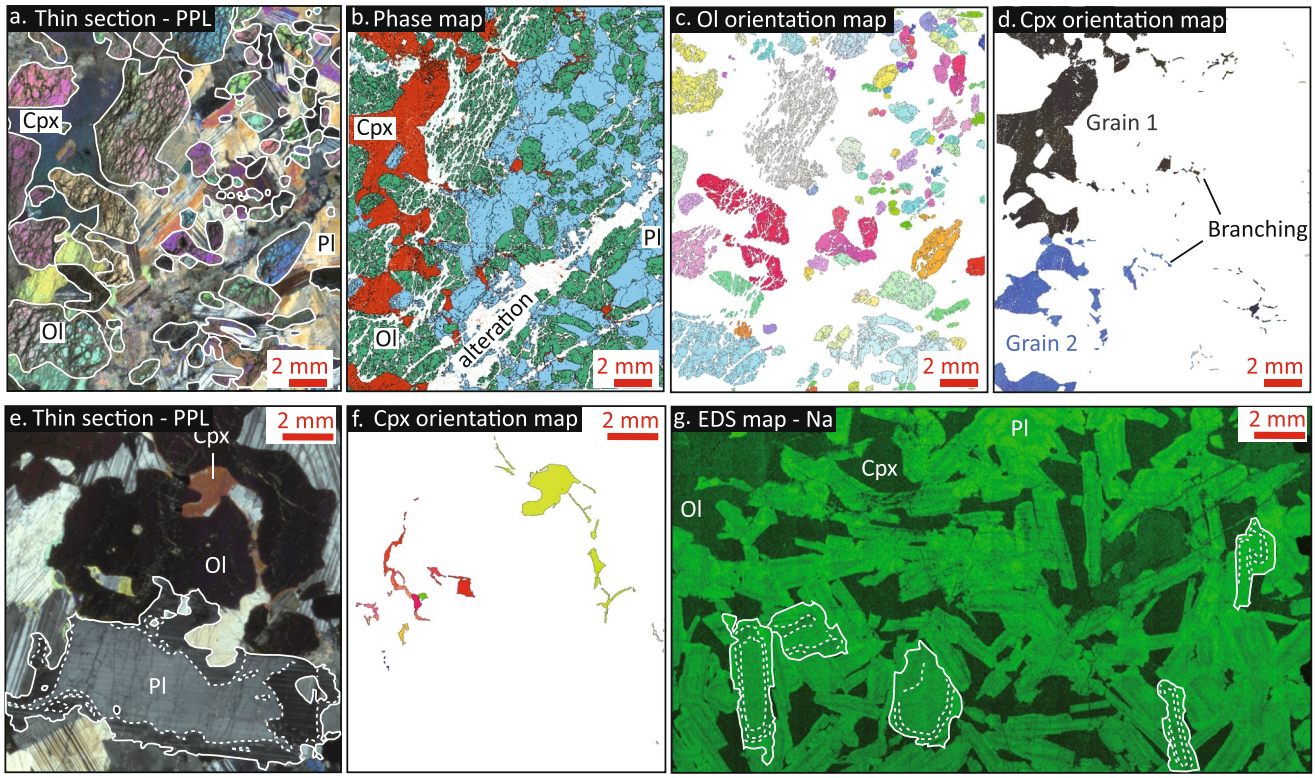

Figure 4. Selected results obtained by EBSD measurements on the Ol-rich sample 153-923A-12R-1W, 74–77 cm (a–d), the troctolite 153-923A-12R-1W, 118–121 cm (e–f), and (g) the poikilitic gabbro 153-923A-16R-1W, 89–91 cm. (a) Microphotograph of the mapped area (see description in Figure 3). (b) Phase map with grain boundaries highlighting the greater alteration of Ol-rich samples (white areas). (c) Ol orientation map showing the random organization of the Ol crystal matrix that lack crystal-plastic deformation evidence (e.g., kink bands). (d) Interstitial Cpx originating from the two main poikilitic Cpx cores evidenced by the Cpx orientation map. (e) Microphotograph of the mapped area showing a coarse-grained Pl with complex zoning and chaotic grain boundaries. (f) Cpx orientation map showing the interstitial character of Cpx grains and branching from the main Cpx core. (g) Energy Dispersive Spectrometry map for Na highlighting the systematic complex zoning recorded in a typical Pl matrix of "poikilitic gabbros" (Cannat, Karson, & Miller, 1995).

grain boundaries, typical of the Ol crescumulate textures described by Cannat, Karson, and Miller (1995). It mainly embeds Pl chadacrysts. Small interstitial Cpx are found in two areas in between the Ol as "branches." The two Cpx are thin interstitial layers along the Ol grain boundary (min. 7 mm long, Figures 4e and 4f). Other Cpx grains found in the rest of the sample also present these characteristic interstitial features. Plagioclases are medium to coarse grained, euhedral in shape, and present very complex zoning. Grain boundaries are also highly irregular, almost lobated, crosscutting the main twin direction.

The lower unit is characteristic of the poikilitic gabbros described by Cannat, Karson, and Miller (1995). Troctolite and Ol gabbros with contrasting Ol textures were collected at 65 mbsf along a ∼100 cm-long core. The transition from one lithology to the other is rapid but diffuse. Pl characteristics are the same in all samples. Plagioclase grains are medium-grained subhedral laths showing magmatic and a few deformation twins (Figures 2j, 2n, and 2q). Some grains are more globular, and all present complex zoning (Figure 4g). Plagioclase was the dominant phase for all four samples collected. Pl grains are randomly oriented, and form the main structure of the cumulates. Olivines are medium to coarse grained, with textures similar to the crescumulate textures described earlier (Figures 2p and 2q). They are interstitial to the Pl, present angular shapes, and more rounded grain boundaries when in contact with Cpx. The difference in Ol textures described in hand samples is caused by the size and associated lobate texture of the grains. Medium grained Ol are less lobated, and less interstitial than coarser grains. The Cpx content varies between samples, but the textures remain similar. Their grain size varies from almost pegmatitic with large poikilititic grains embedding Pl to more medium grained and interstitial in between Pl laths. Poikilitic Cpx locally display intergrowths.

4.2. Microstructures and EDS Maps of ODP Hole 923A Samples

The fabric of all samples is weak, which is consistent with other slow-spreading ridge observations (Allard et al., 2021; Boulanger et al., 2021; Ferrando, Basch, et al., 2021). No Ol or Cpx fabric can be observed due to the small number of grains analyzed per thin section (Table S2 in Supporting Information S1). Pl only presents weak but typical axial-B type fabric in the top two samples (Ol gabbro and troctolite 153-923A-8R-1, 31–34 cm and 153-923A-8R-1, 40–47 cm, respectively) with J indexes (using grain average orientations) varying between 1.87 and 2.39 (Table S2 in Supporting Information S1). The GOS of Pl is overall low (0.75° on average, see Section 3.2). As described in Section 4.1, crystal-plastic deformation is more pronounced in the middle coarse-grained sample (Ol-bearing gabbro 153-923A-11R-2, 74–76 cm) with an average GOS of 1.31. Overall, the fabric recorded in all samples is consistent with an origin from weak compaction (similar to the one found in Ferrando, Basch, et al., 2021). There is no clear evidence for intrusive events in the sequence except maybe for the top two samples presenting the axial-B type fabric, but additional (geochemical) evidence is required to assess this. Finally, the Ol fabric provided here on only one Ol-rich sample (153-923A-12R-1, 74–77 cm) and the resolution of these data do not allow us to draw similar conclusions to those in Drouin et al. (2010) and Ferrando et al. (2018) regarding a potential mantle origin of the disrupted Ol-rich matrix partially assimilated to form this sample.

Apart from the crystal fabric, some characteristics emphasized by the EBSD maps are worth noticing. The Ol orientation in the Ol-rich sample cannot be quantified by EBSD due to the small number of grains, but it seems random from the observation of the orientation maps (see Figure 4c). The map highlights the rounded character of the grains and the very high Ol concentration in some areas of the thin section. EBSD data also confirm the pegmatitic character of the poikilitic Ol grain in troctolite 153-923A-12R-1, 118–121 cm with similar resorbed grain boundaries (Figure 4e). The interstitial Cpx observed mostly in the Ol-rich or troctolitic samples are in fact ramifications of larger Cpx cores, as observed in Ol-rich sample 153-923A-12R-1, 74–77 cm and troctolite 153-923A-12R-1, 118–121 cm. These ramifications are found 7 mm away from their core and are either coating Ol grains or interstitial to the main Pl matrix (Figures 4d and 4f). In other samples, the ramifications are not observed but groups of small interstitial Cpx grains seem to share similar orientations (e.g., troctolite 153-923A-8R-1, 31–34 cm and Ol gabbro 153-923A-8R-1, 40–47 cm). Finally, the EDS maps reveal a significant zoning of Pl grains visible in the Ca and Na maps. The zoning recorded is rather concentric and complex with up to three visible rim generations. These rims are mostly Ca-rich towards the cores and Na-rich in the outer rim with the widespread presence of locally truncated and resorbed contacts (Figure 4g). The imperfect but concentric geometry of the zoning suggests crystallization from a magma rather than dissolution-reprecipitation during viscous deformation (Holness et al., 2017). Complex zoning is found in (almost) all crystals from the lower unit and the troctolite of the middle unit. In the upper unit, the complex zoning is mostly present in the fine-grained domains and disappears in the lowermost coarse-grained gabbro and in the top troctolitic gabbro, where only the few coarser grained Pl are zoned.

4.3. In Situ Geochemistry

All acquired data during this study are compared with either shipboard or post-cruise data available for each drilled site. Data are compiled from Ross and Elthon (1997), Fujibayashi et al. (1997), Koepke et al. (2005), Miller et al. (2009), Drouin et al. (2009), Ferrando et al. (2018), Tamura et al. (2008), Niida (1997), and Coogan et al. (2000). This study focuses on the main cumulate forming minerals, that is, Ol, Pl and Cpx.

4.3.1. Major and Minor Elements

Overall, the samples from the 70-m-long section in ODP Hole 923A and the fourteen analyzed samples from the 400 m-long section from IODP Hole U1309D record almost the entire range of compositions of both drilled sections. Samples collected in Hole 923A present more primitive mineral assemblages than samples from Hole U1309D, with mostly Ol gabbros and troctolites, yet their compositions span about the same compositional range (Figures 5–7, Table S1 in Supporting Information S1).

Ol from Hole U1309D have Mg# of 70–83 (Figure S1 in Supporting Information S1), with NiO contents varying between 0.06 and 0.24 wt% and MnO contents between 0.23 and 0.43 wt%. The Ol-rich sample 305-U1309D-228R-4, 43–46 cm is the most primitive, with the highest Mg# and NiO contents of Ol of 83 and 0.19 wt% on average, respectively (Figure 6d). Ol from Hole 923A have Mg# of 68–85, NiO contents between 0.05 and 0.23 wt% and MnO contents between 0.12 and 0.45 wt% (Figure 6d). The minerals from Ol-rich sample 153-923A-12R-1, 74–77 cm are the most primitive, with an average Mg# of 84.5, NiO content of 0.2 wt% and MnO

10.1029/2023GC011409

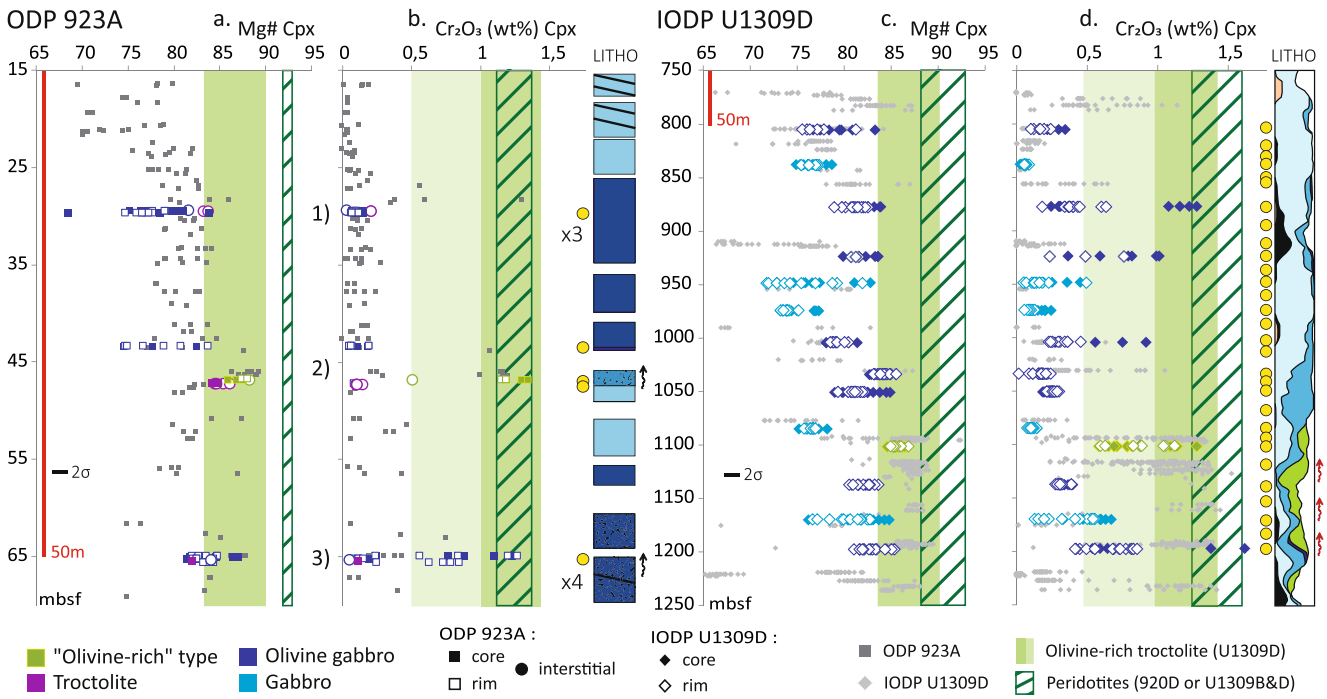

Figure 5. Clinopyroxene (a) Mg# (=100 × Mg/(Mg + Fe) molar) and (b) Cr_2O_3 (wt%) compositions of ODP Hole 923A samples. Cpx (c) Mg# and (d) Cr_2O_3 (wt%) compositions of analyzed samples from IODP Hole U1309D between 800 and 1,200 mbsf. 2σ errors inferior to the symbol size for Cr_2O_3 (wt%). Lithology: see Figure 1. Colored symbols: single analysis from this study. Gray symbols: data from previous studies (see Section 4.3). Green area: variation range of Ol-rich troctolite data from Drouin et al. (2009) and Ferrando et al. (2018). Green hatched area: variation range of peridotite data from ODP hole 920D (Niida, 1997) and IODP hole U1309D (Tamura et al., 2008).

content of 0.25 wt%. On the first order the overall compositional evolution seems to follow a fractional crystallization trend with very narrow ranges of Fo content for each individual sample, and variations of maximum 2 mol% Fo in Hole 923A and 3 mol% in Hole U1309D (Figure 6d).

Pl from both Holes U1309D and 923A span a large range of An contents of 52–88. Pl from the Ol-rich samples are on average slightly more primitive (Figures 7a and 7b). Figure 7 also shows the strong variability in An contents recorded in every sample, that spans 3–19 mol% in Hole U1309D and 11–25 mol% in Hole 923A. This variability can be observed at the thin section scale through the complex zoning of Pl grains, zoning that tends to be more developed in samples from Hole 923A (Figure 4g and maps in Table S2 of Supporting Information S1, see section above). There is no clear downhole evolution trend in the An content in Hole U1309D (Figure S1 in Supporting Information S1), which discards the formation of the 800–1,100 mbsf as a single "fractionation cycle" as postulated by Suhr et al. (2008), who already described this model as "simplistic."

Cpx Mg# from U1309D samples range from 72 to 87 (Figure 5c), and from 75 to 88 in samples from Hole 923A, with one Cpx outlier at 68 (Figure 5a). Both Ol-rich samples 153-923A-12R-1, 74–77 cm and 305-U1309D-228R-4, 43–46 cm present Cpx compositions that fall in the range of Ol-rich troctolite samples from Drouin et al. (2009) and Ferrando et al. (2018), with Cpx Mg# between 84.5 and 88.2. Their Cr_2O_3 contents vary between 0.50 and 1.34 wt% (Figure 6c), thus reaching the Cr_2O_3 values recorded in Ol-rich troctolites and in Cpx from peridotites sampled in both AM and KM areas (Niida, 1997; Tamura et al., 2008). Olivine gabbros from both sections present Cpx with high Cr content, up to 1.38 wt% Cr_2O_3 in 305-U1309D-249R-1, 58–62 cm (located at the bottom of the section, Figure 5d), and up to 1.23 wt% Cr_2O_3 in 153-923A-16R-1, 24–27 cm of Hole 923A (Figure 5b). The Cr contents are lower in gabbros that are only found in Hole U1309D (between 0.03 and 0.67 wt%) but are also low in the troctolite samples from Hole 923A (between 0.09 and 0.20 wt%). TiO_2 contents show similar tendencies in both Holes U1309D and 923A, and overall vary between 0.18 and 1.80 wt% (Figure 6a). The majority of Cpx cores whose Mg# values range between 78 and 87 have TiO_2 content below 0.60 wt%. Below Mg# 78, TiO_2 contents of Cpx increase up to 1.20 wt% for both mineral cores and rims. Above Mg# 78, the TiO_2 content of Cpx is higher in mineral rims than cores and reaches values up 1.41 wt% in Ol gabbros and up to 1.46

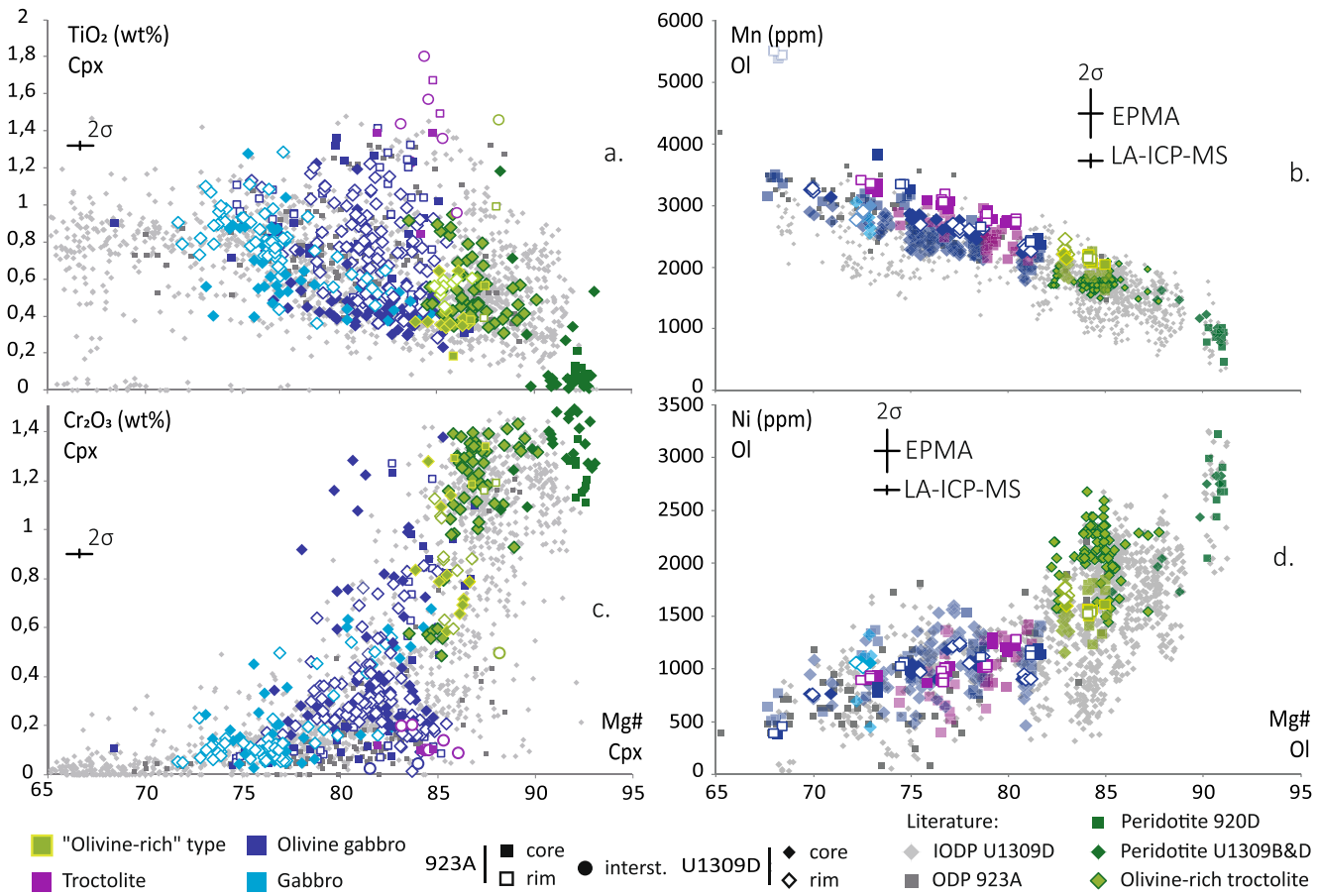

Figure 6. Mg# vs. (a) TiO_2 wt% and (c) Cr_2O_3 wt% in Cpx. Mg# vs. (b) MnO wt% and (d) NiO wt% in Ol. Colored symbols: single analysis from this study. No distinction between Ol cores and rims is provided for the EPMA analyses (large transparent points), but are provided for the data obtained by La-ICP-MS. Gray symbols: data from previous studies (see references in Figure 5).

wt% in interstitial rims of Ol-rich samples. The highest TiO_2 contents (between 1.4 and 1.8 wt%) are recorded in the troctolite 153-923A-12R-1, 74–77 cm, for associated Mg# of 84 on average. These are the highest Cpx TiO_2 contents analyzed so far in Cpx from both sampling sites (Figure 6a).

The minimum, average and maximum values of Fo contents in Ol and Mg# in Cpx and Pl An contents are compared in Figures 7a and 7b. Overall, the average point per sample falls in or close to the slow-spreading areas of the diagram (Kane FZ and SWIR from Kvassnes et al., 2004). The An contents of Pl show more variability than the Fo contents of Ol (Figure 7a) and the Mg# of Cpx (Figure 7b), and the more primitive mineral assemblages (Ol-rich samples and troctolites) record narrower variation ranges of Cpx Mg# compared to other samples (Ol gabbros and gabbros). The data are compared to the composition of the mineral assemblages obtained during fractional crystallization of a primary MORB-type melt for the AM system modeled with MELTS (BG from Godard et al., 2009, see Table S5 in Supporting Information S1). The comparison shows a systematic shift of the data towards lower An content of Pl for all samples and/or higher Mg# of Cpx and Fo contents of Ol. The slope of the evolution trend described between the most primitive Ol-rich sample and the most evolved gabbro one is also significantly different compared to the modeled FC trend, which goes towards lower Cpx Mg# at similar Pl An contents.

4.3.2. Trace Elements

The trace element contents of the main gabbro-forming minerals are consistent with previously published data for both Holes 923A and U1309D. The variability found in each section corresponds to the full variation range previously found in each borehole (Figure 8). Overall, the two sections from Holes 923A and U1309D present

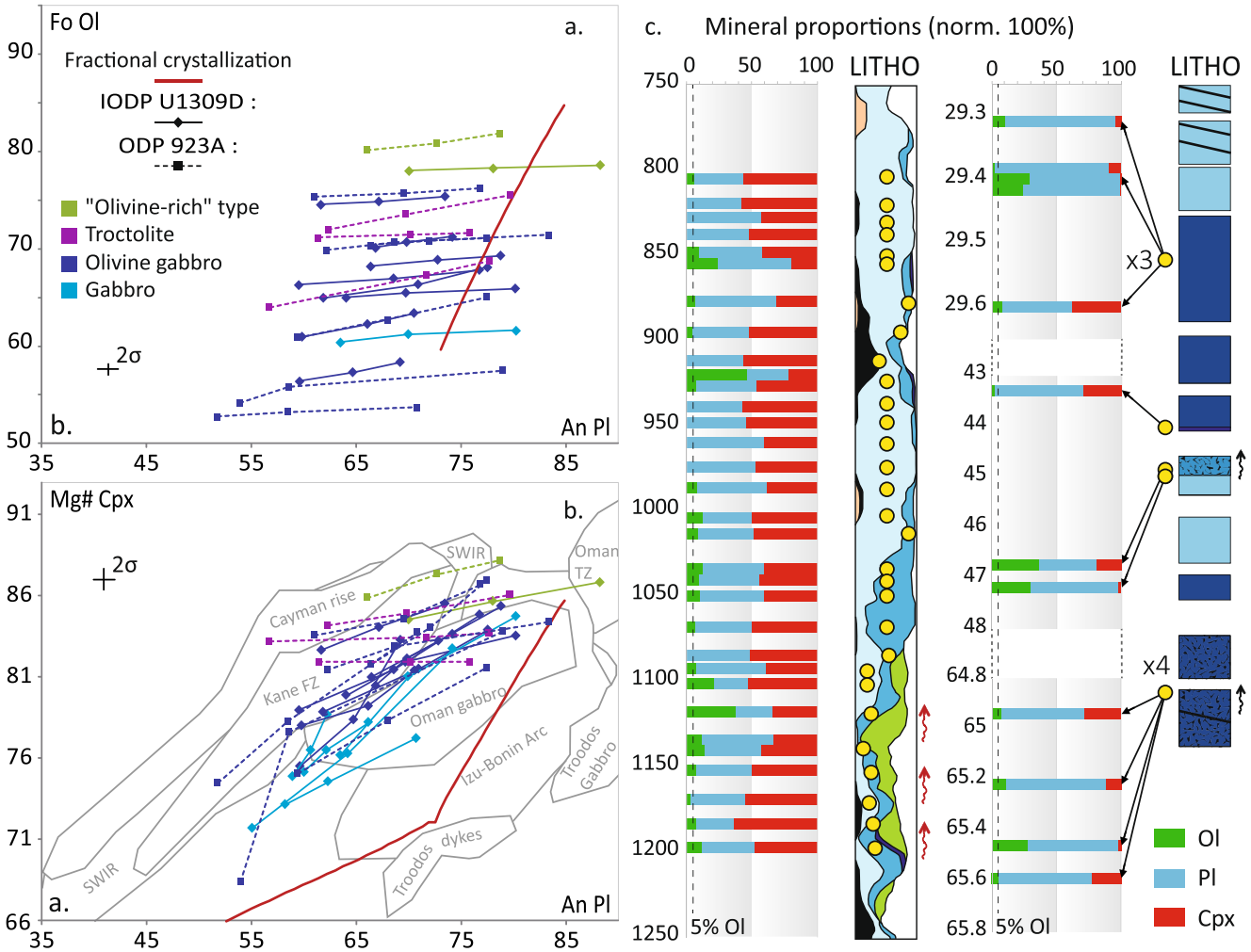

Figure 7. Pl An content vs. (a) Ol Fo content and (b) Cpx Mg#. MELTS fractional crystallization model (1 wt% H_2O and QFM0) for solid line of descent of the BG composition from Godard et al. (2009, Table S5 in Supporting Information S1). Pl and Cpx data compared to gabbros from different areas (from Kvassnes et al. (2004), references therein). (c) Sample modes with associated downhole sample locations (see Figure 1).

noticeable differences in the main evolution tendencies despite similar recovered lithologies. Significant differences exist depending on the type of lithologies considered, that is, Ol-rich samples and other gabbros.

Ol from Hole 923A present significant enrichments in REE in the Ol gabbro samples, with Yb_N (N, normalized to CI chondrite, McDonough & Sun, 1995) reaching up to 2.77 (ranging from 0.38). The fractionation between MREE and HREE are overall low with Dy_N/Yb_N mostly below 0.05 with two outliers that have $Yb_N < 0.5$ and associated Dy_N/Yb_N of 0.1 and 0.12 (Figure 8a), similar to the fractionation recorded in Ol-rich troctolites from Hole U1309D (Drouin et al., 2009; Ferrando et al., 2018). Ol-rich samples and troctolites present a low fractionation range (Dy_N/Yb_N below 0.06) and Yb_N reaching only up to 1.39 for troctolites and 0.7 for Ol-rich samples. On the other hand, most of Hole U1309D Ol present low Yb_N below 0.8, and fractionation that span a relatively larger range of Dy_N/Yb_N values between 0.015 and 0.07 (Figure 8b), which correspond to the range of previously analyzed Ol from the section and in Ol-rich troctolites. Gabbros present higher Yb_N (0.5–0.8), and Ol-rich samples present low Yb_N but significant fractionation up to 0.2 Dy_N/Yb_N, similar to the fractionation recorded in peridotite Ol from AM (Figure 8b). For both sections, the Co (180–229 ppm in Hole 923A and 166–239 ppm in Hole 1309D, Figure S5f in Supporting Information S1) and Zn (115–239 ppm in Hole 923A and 102–236 ppm in Hole 1309D, Figure S5g) contents of Ol are higher than the peridotite range from Rampone et al. (2016) and Sanfilippo et al. (2014, 2015). The Ol gabbro values from the same studies represent the lower bound of the range spanned by the data presented here.

10.1029/2023GC011409

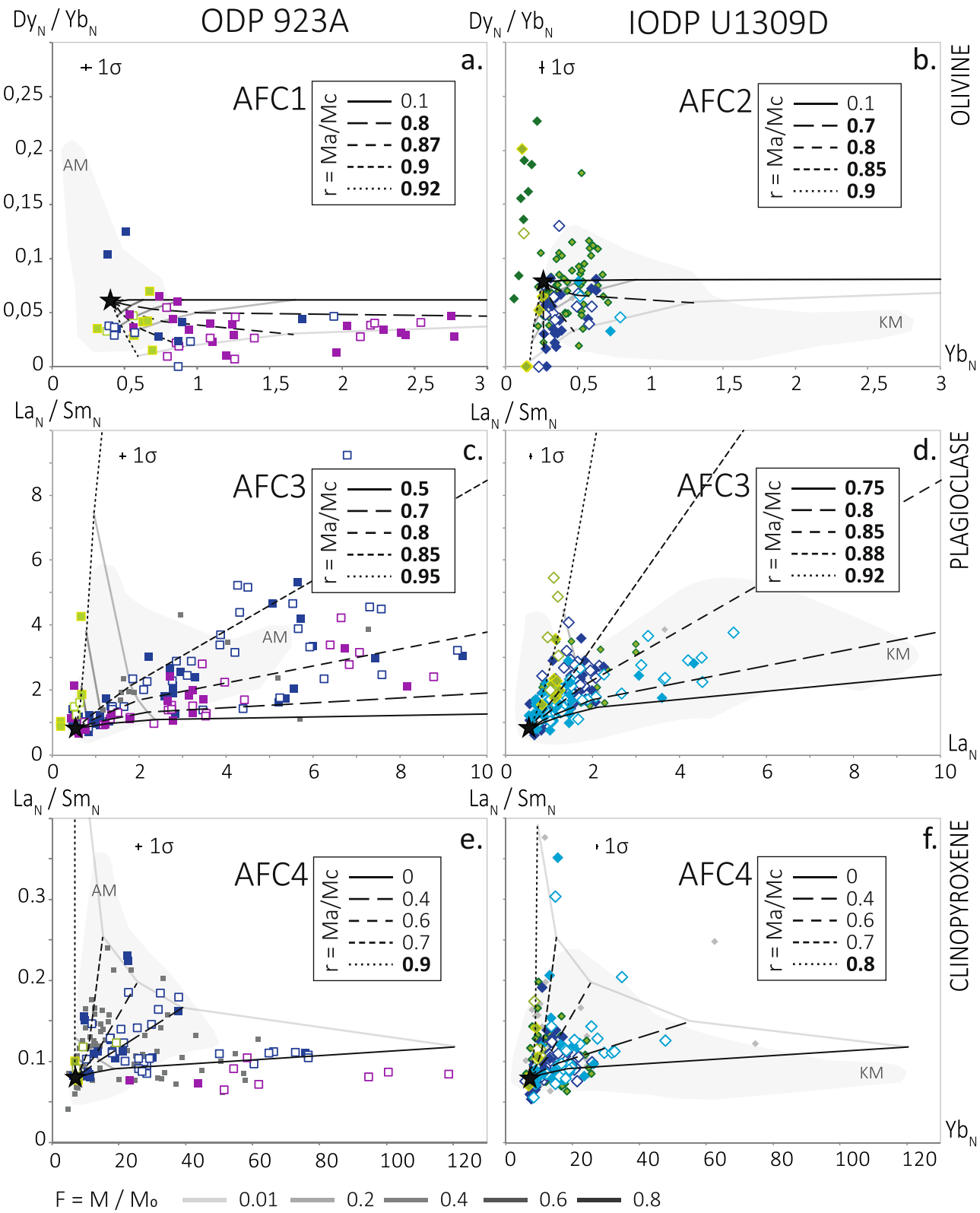

Figure 8.

Pl from both sections present similar compositions (Figures 8c and 8d). Ol-rich samples from Holes 923A and U1309D present the lowest La_N (below 1.25), and the highest LREE/MREE fractionations with La_N/Sm_N of up to 5.48. Olivine gabbros and troctolites from Hole 923A show La_N compositions ranging from 0.44 to 9.45, the highest enrichment identified in the hole so far, and increasing La_N/Sm_N with La_N ranging from 0.41 to 5.34 (with one outlier at 9.23, Figure 8c). Olivine gabbros from Hole U1309D present relatively clustered values compared to Hole 923A, with La_N ranging between 0.57 and 2.26 and La_N/Sm_N between 0.62 and 4.02 (Figure 8d). These data fall in the range of compositions of Ol-rich troctolites from the literature. Most of the gabbros Pl fall in the same range, yet some Pl cores and mostly rims present higher enrichments in LREE with La_N between 2.7 and up to 5.25. La_N and La_N/Sm_N lack progressive increases at decreasing An content of the Pl. 89% of Pl from both sections span a constant range of 0.2–2.35 ppm La_N and 80% a constant range of 0.62–2.66 La_N/Sm_N at decreasing An contents between 80 and 60.

Cpx from Hole 923A record higher REE enrichments compared to minerals from Hole U1309D, and the highest compared to available data for slow-spread oceanic crust samples. Yb_N range between 6.5 and 118.6, with Ol-rich samples presenting $Yb_N < 19.3$ (highest enrichment recorded in troctolites, Figure 8e). Associated LREE/MREE fractionations represented here by La_N/Sm_N vary between 0.07 and 0.23. For Hole U1309D, Cpx present lower enrichments with Yb_N varying between 5.9 and 47.7, the Ol-rich sample showing values below 10.4. In contrast, the majority of Cpx from gabbros and Cpx rims from Ol gabbros and gabbros present the stronger enrichments in Yb_N above 15 (Figure 8f). The associated fractionation and La_N/Sm_N values range between 0.05 and 0.35, and overall are stronger than those recorded in Hole 923A. Taken individually, within each sample, the evolution trend for Cpx is marked by strong fractionation for relatively constant La values in Hole U1309D, while it is the opposite for Hole 923A samples (strong enrichments for relatively low fractionation). As observed in Pl, Cpx from both sections present no increase in both Yb_N and La_N/Sm_N with decreasing Mg#. Cpx from both sections present negative Eu anomalies (<0.98), with almost systematically lower Eu/Eu* recorded in Cpx rims than in cores (Figure S5a in Supporting Information S1). In addition, most of the Cpx rims in Hole 923A reach lower Eu/Eu* than in Hole U1309D (0.18–0.94 in Hole 923A and 0.46–0.98 in Hole U1309D). Most of the incompatible Zr contents in Cpx are similar between the two sections, with an increase of the lower bound of the range spanned at decreasing Mg# (from ∼4.5 ppm at Mg# 86 to ∼18 ppm at Mg# 74, Figure S5d in Supporting Information S1). On average, Cpx rims are richer in Zr than cores in both sections, yet some reach much higher values in Hole 923A (858 ppm) than in Hole U1309D (94 ppm). Finally, slightly compatible Co contents progressively increase with decreasing Mg# (∼29 ppm at Mg# 87 and ∼57 ppm at Mg# 75), with overall higher values by 10–15 ppm at equivalent Mg# in Hole U1309D compared to Hole 923A (Figure S5c in Supporting Information S1).

5. Discussion

5.1. Evidence for Melt-Mush Reactions

5.1.1. Sample Textures

The study of the gabbroic lithologies (gabbro, Ol gabbro, troctolite) sampled on average every 15 m in both Hole 923A and Hole U1309D substantiates the strong textural variability present in both sections. This is best exemplified in Hole 923A by the poikilitic gabbro (sensu lato) intervals surrounded by undifferentiated "brown-pyroxene" gabbros (Cannat, Karson, & Miller, 1995; Coogan et al., 2000), and by the Ol habit that ranges from angular grains aggregate to lobate Ol crystals with branching and dendritic crescumulates (Cannat, Karson, & Miller, 1995). Without considering grain size variations that add to the textural variability, Hole U1309D samples are mostly characterized by the variably poikilitic textures of Pl, and mostly Cpx grains. Ol-bearing gabbro 305-U1309D-243R-2, 23–27 cm is an extreme endmember that only contains very coarse-grained (almost pegmatitic) Cpx oikocrysts, a texture already observed at KM by Lissenberg and Dick (2008).

Figure 8. Variations in trace element contents versus trace elements ratios in (a) and (b) Ol crystals (Yb_N vs. Dy_N/Yb_N), (c) and (d) Pl crystals (La_N vs. La_N/Sm_N), and (e) and (f) Cpx crystals (Yb_N vs. La_N/Sm_N) from ODP Hole 923A (a), (c), and (e) and IODP Hole U1309D (b), (d), and (f). The legend for the colored and gray symbols is provided in Figure 5. The propagated errors for each graph are smaller than the symbol size. Gray areas: Kane Megamullion (KM) or Atlantis Massif (AM) data for comparison. Black stars: equilibrium crystal composition with the primitive reacting melt used in the AFC models (black dashed lines). F: ratio between the magma mass at a given step and the initial magma mass prior to reaction, *r*: ratio assimilation rate to crystallization rate (DePaolo, 1981).

The samples also present characteristic textures that suggest widespread episodes of (partial) mineral resorption during the formation of the cumulates. Ol and Pl are the two minerals that present the most resorbed textures, either in the form of rounded grains or grains with irregular grain boundaries, sometimes crosscutting other crystallographic features such as Pl twins (see the detailed descriptions in Section 4 and in Figures 2–4). On the other hand, mostly Pl and Cpx seem to crystallize during or past a resorption episode, with the presence of well-defined complex zoning of Pl and the poikilitic textures of both Pl and Cpx grains enclosing resorbed (Ol or Pl) chadacrysts. These textures are characteristic of melt-mush reactions, and they have been observed in other slow-spreading crust gabbros, Ol gabbros, and troctolites (see the review of textures provided in Boulanger & France, 2023 and references therein; Gardner et al., 2020, 2023). In detail, there are some systematic differences in the textures found in the most primitive and the most evolved samples, but also between samples from Hole 923A and Hole U1309D that seem to be associated with melt-mush reaction features.

Both Ol-rich samples present areas composed of a matrix of heavily rounded Ol grains surrounded by poikilitic up to interstitial Pl and Cpx (305-U1309D-228R-4, 43–46 cm and 153-923A-12R-1, 74–77 cm, Figure 3). Other areas in the thin sections present mostly rounded Pl ± Ol chadacrysts within similar coarse-grained Cpx oikocrysts. Resorbed chadacrysts suggest strong Ol assimilation, and to a lesser extent Pl assimilation. On the contrary, the presence of poikilitic Pl and Cpx around the resorbed chadacrysts suggests their crystallization during or past interactions (Figure 3). In Ol-rich sample 153-923A-12R-1, 74–77 cm, Cpx presents characteristic branching, implying late crystallization close to the solidus (Figure 4d). More evolved samples (either troctolites, Ol gabbros or gabbros) still show rounded Ol grains, but present also more evidence for Pl assimilation in the form of rounded Pl grains, well-developed complex zoning in Pl and resorbed Pl chadacrysts in Cpx (Figures 2 and 4). Cpx intergrowths are also common in those samples, which are overall less interstitial but still poikilitic in many samples, and suggest mostly Cpx crystallization during the reactions (see the detailed descriptions in Section 4).

Differences between the two holes mainly reside in the stronger textural variability recorded in Hole U1309D (for which the sampled section is longer), and in the more developed Pl cumulate framework (±Ol) observed in Hole 923A samples. In Hole 923A, Pl are not poikilitic (except in the Ol-rich sample), and Cpx tend to be more interstitial than in Hole U1309D. These discrepancies do not drastically change the modes involved during reactions, yet they might indicate different assimilation/crystallization dynamics in the two magmatic systems.

5.1.2. Geochemical Evidence for Melt-Mush Reactions

5.1.2.1. Variability in the Assimilated Components

Most of the geochemical signatures of the two sections are similar to signatures described as resulting from melt-mush reactions in oceanic crust samples (e.g., Basch et al., 2024; Ferrando, France, et al., 2021; Lissenberg & MacLeod, 2016; Zhang et al., 2020). It consists of the strong decoupling between major and trace elements of the main cumulate-forming minerals, as best illustrated by the high Mg# of Cpx associated with high TiO_2 contents (up to 1.46 wt% at Mg# of 88.2 in the Ol-rich sample of Hole 923A, up to 1.22 at Mg# 81.6 in an Ol-gabbro sample of Hole U1309D, Figure 6a). The major and trace elements decoupling is typical of open reactive environments (Godard et al., 1995; Vernières et al., 1997). Highly incompatible elements represent the composition of the melt, while less mobile elements (compatible elements, heavy REE) are controlled by the reactions. For example, major elements are "buffered" by the surrounding mineral matrix during melt-mush reactions (Coogan et al., 2000), while incompatible trace elements remain in the melt. It has been exemplified experimentally by Yang et al. (2019), who studied the reaction of a relatively evolved melt compared to a primitive crystal matrix that leads to the formation of high-Ti high-Mg# Cpx-saturated melts. The decoupling is also visible for REEs in our samples, for example, Yb versus Mg# in Cpx or La versus An content in Pl (see Figures S5b and S5e in Supporting Information S1, Boulanger et al., 2020).

Locally, some Cpx from the Ol-rich samples and some of the Ol gabbros of both sections are enriched in Cr, reaching values of up to 1.38 wt% in an Ol-gabbro Cpx (Figures 5b, 5d and 6c). These values are similar to the highest values recorded in Ol-rich troctolites from Hole U1309D and Cpx from peridotites (sensu lato) from both KM and the AM areas (Casey, 1997; Niida, 1997; Tamura et al., 2008). The high-Cr signature is also present in a single Cpx oikocryst from Hole U1309D Ol gabbro 305-U1309D-180R-2W, 90–94 cm, with Cr_2O_3 between 1.08 and 1.28 wt% and Mg# varying between 79.7 and 81.3, while the rest of the Cpx Cr_2O_3 range between 0.18 and 0.67 wt% at similar Mg# (78.8–83.9). The textures of the associated samples with highly poikilitic (enclosing resorbed Pl chadacrysts) or interstitial Cpx grains suggest in situ crystallization from a melt rather than an

inherited origin of the minerals (as xenocrysts or antecrysts). The formation of high-Cr Cpx-saturated melt could result from previous interaction of percolating melt with either early formed (Cr-spinel-bearing) cumulates as previously discussed in Lissenberg and MacLeod (2016), or surrounding mantle lithologies.

High-Cr Cpx are present in the Ol-rich sample of both sections, which have strong similarities in textures with Ol-rich troctolites from Hole U1309D (Drouin et al., 2010; Ferrando et al., 2018; Suhr et al., 2008). In Hole U1309D, the Ol-rich sample is located within the Ol-rich interval 4 described by Drouin et al. (2009) and Ferrando et al. (2018, 2020), where they infer the assimilation of harzburgitic mantle into the magmatic sequence. At shallower depths in Hole U1309D, the high-Cr signatures are also found in samples located in the vicinity of more primitive lithologies (Figure 1b), even though direct association with mantle lithologies cannot be drawn here or for Hole 923A samples. Migrating melt would have inherited the high compatible element concentrations of assimilated phases, whether it originates from the mantle wall-rock or early primitive cumulates, and Cr would have later been quickly incorporated in Cpx during crystallization (compatible for Cpx, $D_{Cr} = 3.8$, Bédard, 2001).

In Hole 923A, the four poikilitic Ol gabbro samples in Hole 923A are only separated by 20 cm on average (between 64.94 and 65.59 mbsf). The high-Cr signatures of interstitial Cpx found in the top and bottom Ol gabbros disappear towards the two samples in the center of the section (Figure 5b). We interpret this very local presence of the high-Cr Cpx signatures as a consequence of heterogeneous transport of reactive melt through the mush, even at the dm scale. This is in line with previous observations of more evolved lithologies (Coogan et al., 2000; Sanfilippo et al., 2020). Overall, melt percolation through the reservoir at Kane Megamullion and Atlantis Massif was likely heterogeneous. It involved reactions between local migrating melts and different materials, either cumulates at variable degrees of differentiation or even potentially from the mantle, thus contributing to the variety of textures and compositions recorded in both sections.

5.1.2.2. Variability in the Melt-Mush Reaction Regime

Another key geochemical signature indicative of melt-mush reactions in minerals is the higher fractionation between incompatible trace elements compared to their enrichment, which deviates from typical fractional crystallization trends. During crystallization, the incompatible elements fractionate and the concentrations increase with the degree of differentiation. Here, the most primitive lithologies (Ol-rich samples and some Ol gabbros) present the stronger fractionation and associated low enrichments in REEs. For example, Ol-rich samples of Hole U1309D have Pl with La_N/Sm_N of up to 5.47 for La_N <1.25, whereas Pl of the most evolved gabbros reach La_N/Sm_N of up to 5.25 for La_N of 3.8 (Figure 8d). Similar conclusions can be drawn for Hole 923A Pl, with stronger fractionation but mostly enrichments recorded in the Ol gabbros and troctolite samples (La_N/Sm_N of up to 5.65 and La_N of up to 9.45, Figure 8c).

There are also significant differences between Hole 923A and Hole U1309D depending on the mineral considered. The Ol signatures are the most discriminating, with Ol from Hole U1309D presenting strong Dy_N/Yb_N variability at almost constant Yb_N (below 0.79, Figure 8b). In contrast, Ol from Hole 923A show lower Dy_N/Yb_N values, and an evolution from primitive to evolved cumulate assemblages towards high Yb_N (up to 2.77, Figure 8a). Pl compositions in both sections show similar fractionation ranges between 0.9 and 5.57 La_N/Sm_N (with one outlier in Hole 923A at 9.23 La_N/Sm_N). In Hole U1309D, the higher fractionations are recorded in the Ol-rich samples, and most present La_N <2.26, except for gabbros that show La_N up to 5.25 (Figure 8d). In contrast, in Hole 923A the higher fractionations are recorded at higher La contents, whereas two trends can be distinguished at La_N <2: one characteristic of the Ol-rich sample and most Ol gabbros evolution that present almost constant La_N and increasing La_N/Sm_N, and a second for some Ol gabbros and the troctolite samples with progressively increasing La_N/Sm_N with La_N (Figure 8c). Cpx signatures resemble more those of Pl as both holes are globally consistent, with slightly higher fractionation recorded in Hole U1309D (La_N/Sm_N of up to 0.35 in gabbros), and higher REE enrichments recorded in Hole 923A (Yb_N of up to 118 in Ol gabbros and troctolites, Figures 8e and 8f). Notably, the Ol-rich samples of Hole 923A do not present REE fractionated signatures at constant REE contents, and follow the evolution trend of other lithologies. All available Cpx data from Hole U1309D Ol-rich troctolites present the same range as the minerals analyzed here. However, they do not overlap with the most enriched and fractionated compositions of Cpx rims in gabbros (Figure 8e).

To summarize, there are some noticeable discrepancies between the interaction signatures recorded in different minerals, lithologies, and crustal sections. Hole U1309D presents slightly more fractionated REE signatures, particularly for the most primitive lithologies, and lower enrichments even in gabbros that are more evolved

mineral assemblages compared to Hole 923A olivine gabbros and troctolites. These geochemical discrepancies can originate from different factors, in particular the composition of the reactive melt and the nature of the assimilated mineral assemblage. The reaction regime itself also plays a prominent role in shaping compositions, whether assimilation-dominated or crystallization-dominated (i.e., the mass of material added or extracted from the reactive melt). Based on previous studies in oceanic systems (e.g., at Atlantic Bank, Boulanger et al., 2021; Boulanger & France, 2023; Zhang et al., 2020, or at the Doldrums Megatransform System, Basch et al., 2022), REE evolution towards stronger fractionation can be associated with assimilation-dominated reactions, mainly observed in the most primitive lithologies. In contrast, strong enrichments argue in favor of crystallization-dominated reactions occurring mainly in the most evolved lithologies. These observations hold for both magmatic sequences, yet it seems that the entire sequence of Hole 923A was subject to preferential crystallization owing to the stronger enrichments recorded in all minerals analyzed. Furthermore, the three investigated minerals form at different stages throughout differentiation, with early Ol formation overlapped by the crystallization of Pl before the later appearance of Cpx. The discrepancies between these different mineral signatures have the potential to document changes in the reactions and/or the regimes of melt-mush reactions during differentiation at both locations.

5.2. Modeling Melt-Mush Reactions

5.2.1. Model Selection

Here, the primary aim of modeling is to test the implication of melt-mush reactions in the acquisition of the mineral REE signatures in both AM and KM.

The magmatic systems considered here are magma reservoirs fed incrementally within mantle wallrock by primitive melt recharges. The full extent at depth of the active reservoirs during differentiation is unknown. We confirm with our additional data that the "fractionation cycle" introduced by Suhr et al. (2008) in Hole U1309D is too "simplistic" due to the heterogeneity of textures and compositions, which do not define any downhole systematics. It is however consistent with sequences built by multiple injections as described, based on the whole rock data, by Godard et al. (2009). The emplaced melts crystallize by progressive cooling with most of the differentiation taking place within a crystal mush, that is, a porous framework of contiguous cumulate minerals (Sparks et al., 2019). Depending on the porosity of the medium, melts are not static and tend to migrate through the system and react with their surroundings (mush minerals and potentially mantle wallrock, see references in the Introduction section). The entire process of melt migration and associated evolution by reaction is reactive porous flow, during which, locally, melt-mush reactions occur. We here distinguish melt-mush reactions from reactive porous flow, as the latter describes a process considering melt migration, hence a process integrating temporal and spatial constraints. Locally, at a given time, a specific melt-mush reaction occurs, and can be characterized by a mineral assimilation stage and a crystallization stage. These two stages can be variably synchronous, and can be recorded to some extent in the mineral assemblage left behind in the cumulates. This is the case in all samples studied here that even record various successive reaction episodes as evidenced by complex Pl zoning.

The motivation behind modeling reactive porous flow and/or melt-mush reaction is to test the impact of the reactions identified texturally in cumulates, and their implication in the acquisition of the characteristic geochemical signatures deviating from crystallization-only trends. Most available models focus on modeling trace elements evolution with two different strategies. The first one considers melt migration spatially. The models allow to track the evolution of a melt through a column during a single reaction and consider a chromatographic effect on element migration during percolation. The model of Reiners (1998) and the Plate model of Vernières et al. (1997) follow this strategy and have been developed for modeling melt transport at low porosity through the mantle. The second strategy focuses on the impact of assimilation and crystallization on the trace element composition of a melt at decreasing melt fractions. This approach is the one of the Assimilation-Fractional Crystallization model of DePaolo (1981), initially developed to track wallrock assimilation in magma chambers.

The complexity of modeling reactive porous flow is that, contrary to magmatic processes occurring in a continuous melt-rich environment where melt homogenization is possible, heterogeneities more likely develop due to changes in melt flow dynamics, enhanced by local changes induced by melt-mush reactions themselves. The variability at all scales in the modes and textures recorded supports this hypothesis in addition to the mineral compositions that are the best archive of melt-mush reactions. Another issue is the lack of quantification of melt-

mush reaction as it relies mostly on complex textural and geochemical observations. Most thermodynamic models consider separately the effect of chemistry and temperature on the assimilation stage, and only a few data exist on changes in the mush porosity induced by melt-mush reactions (Gleeson et al., 2023; Hu et al., 2022). In that case, modeling reactive porous flow is challenging. The results of the Reiners (1998) and the Vernières et al. (1997) models strongly depend on the initial porosity of the system, that is not constrained here, and the input porosity evolution during the reactions, for which we have only little information.

For these reasons, we chose to perform Assimilation-Fractional Crystallization modeling with the equation of DePaolo (1981). The AFC equation has been widely applied to oceanic magmatic systems (Basch et al., 2021, 2022; Borghini & Rampone, 2007; Boulanger et al., 2020, 2021; Coogan et al., 2000; Ferrando, France, et al., 2021; Gao et al., 2007; Lissenberg et al., 2013; Sanfilippo et al., 2014, 2020; Zhang et al., 2020, 2021). It requires as input parameters the initial REE composition of a reactive melt, the composition of an assimilated mineral assemblage, the nature and proportion of phases that crystallize from the reactive melt (and associated REE partition coefficients for each phase), and the "arbitrary" ratio r between the mass assimilation rate and the fractional crystallization rate during the process (DePaolo, 1981).

5.2.2. Modeling Strategy

The minerals record the entire complex evolution story of the active mush reservoirs, whose full extent during differentiation is unknown. As already pointed out, the composition of the melt can also drastically vary over short distances and evolve locally, depending on the crystal matrices it migrates through. Our strategy is to use the AFC model to estimate the best conditions of average reactions that impacted the Ol, the Pl, and the Cpx records individually. By doing so, we aim to test for potential variations in the reaction regimes from the earliest (Ol, then Pl) to the latest (Pl, and finally Cpx) phases formed within the reservoirs. This means that the modeled reactions do not aim at reproducing the instantaneous thermodynamically-constrained reaction occurring during reactive porous flow, but the reaction that best approximates the average assimilation and average crystallization stages during the evolution of the mineral considered. Additionally, we aimed to compare the models obtained for the two crustal sequences in order to test for potential variations in the reaction regimes during the evolution of the gabbroic series.

The sample textures enable us to define the mineral phases and to approximate their relative proportions for the assimilation and the crystallization stages of the reactions (see the description of the reactions below). The composition of the assimilated minerals is defined from the composition of the most primitive mineral cores analyzed in each section, approximating the suspected composition of early formed minerals. Selecting the initial melt composition, which constrains the starting point of the models, is difficult due to the heterogeneity of the samples. To be consistent with the dynamics of the reservoirs, we consider an initially primitive melt. We take the (REE) composition of a theoretical melt in equilibrium with the most primitive of the analyzed minerals (either core or rim). Such equilibrium melts have already been considered in AFC modeling (e.g., Boulanger et al., 2021; Gao et al., 2007; Sanfilippo et al., 2020; Zhang et al., 2020). Finally, the r value representing the ratio between the assimilation rate and the fractional crystallization rate is set to account for the range of REE fractionation in each model. No distinction is made for the assimilation of the more primitive material, because the composition of the melt, the phase proportions, and the reaction regime (assimilation vs. crystallization) are more likely to impact the results than small variations in the mineral REE contents (Boulanger & France, 2023).

5.2.3. Olivine Evolution

Ol textures in the Ol-rich samples and pegmatitic troctolite from Hole 923A suggest strong assimilation during the earliest evolution of the mush in both sections (Figures 2o and 3). While there is less evidence in the more evolved mineral assemblages of Hole 923A, widespread resorption evidence is found in Hole U1309D. Ol presence in more evolved assemblages suggests that Ol crystallizes later in the sequence, even though no crystallization textures can be observed directly associated with resorption features. In contrast, Pl and Cpx textures suggest crystallization during or after the assimilation of Ol (presence of resorbed Ol chadacrysts in Pl and Cpx). We did not find (resorbed) chadacrysts of Pl or Cpx in Ol nor any evidence for concurrent assimilation of Pl and Cpx with Ol, which suggests only crystallization of Pl and Cpx during the evolution of Ol, and only minor Ol crystallization past assimilation. Hence, we selected the following equation for the evolution of Ol by AFC:

$$\text{Hole 923A, AFC1: } Ol_{100} + \text{melt1} \rightarrow Ol_5 + Pl_{80} + Cpx_{15} + \text{melt2}$$

$$\text{Hole U1309D, AFC2: } Ol_{100} + \text{melt1} \rightarrow Ol_5 + Pl_{65} + Cpx_{30} + \text{melt2}$$

The two equations are similar to the reaction described by Ferrando et al. (2018) during Stage 2 of the (dunitized) harzburgite assimilation. The distinct REE evolution trends described earlier in Holes 923A and U1309D suggest different reaction modes during assimilation and crystallization between the two systems. As Ol assimilation is preferentially recorded in the most primitive lithologies, we define a more primitive crystallized assemblage during the reaction at KM. To obtain the significant enrichments recorded in Hole 923A, crystallization of REE-poor minerals is required, consistent with dominant Pl crystallization in AFC1. The strong fractionation at constant REE content in Ol from Hole U1309D requires a similar assimilated component (there is also no textural evidence to suggest otherwise), and is consistent with crystallization of more Cpx, richer in REEs, to prevent REE enrichment of the melt during melt-mush reaction. The r ratios range between 0.8 and 0.92 for Hole 923A, and between 0.7 and 0.9 for Hole U1309D (Figures 8a and 8b). They confirm the strong assimilation during the early stages of reservoir formation in both systems (reproducing the fractionation-only trend of minerals in Ol-rich samples), which is consistent with the local high melt fractions inferred during the formation of Ol-rich troctolites (Basch et al., 2019; Drouin et al., 2010; Ferrando et al., 2018).

5.2.4. Plagioclase Evolution

Pl is the second mineral to form in shallow oceanic reservoirs and is present in all lithologies studied here. Hence, it is likely the best recorder of the reservoir formation (Boulanger et al., 2020). Resorbed Pl chadacrysts in Cpx grains and resorbed Pl cores found in grains presenting complex zoning show evidence for Pl assimilation. Complex zoning also shows that Pl crystallizes during or past resorption episodes. Ol is found either with irregular contact at Pl grain boundaries or as rounded chadacrysts inside Pl grains, suggesting assimilation during melt-mush reactions. The presence of Cpx oikocrysts enclosing resorbed Pl chadacrysts is consistent with their crystallization during melt-mush reactions. Again, no clear evidence for Cpx resorption before Pl crystallization episodes is recorded in the cumulate gabbros, even though it is suggested by thermodynamic models (Boulanger & France, 2023). Pl textures and compositions being similar in both sections, the same reaction is considered for the evolution of Pl by AFC:

$$\text{Hole 923A and Hole U1309D, AFC3: } Ol_{50} + Pl_{50} + \text{melt1} \rightarrow Ol_{25} + Pl_{25} + Cpx_{50} + \text{melt2}$$

The equation is similar to the reaction described experimentally by Yang et al. (2019) for troctolite assimilation. The mode of the assimilated assemblage selected based on the textures is also consistent with Yang et al. (2019) estimates for the dissolved plagioclase to olivine ratios. Here, we selected the lower ratio of 1 considering the higher proportions of Pl in oceanic cumulates. Regarding the mode of the crystallized assemblage, available thermodynamic models suggest higher proportions of crystallized Pl compared to Ol and Cpx during similar reactions (Boulanger & France, 2023). Hole U1309D and Hole 923A show similar evolution tendencies for Pl compositions in all lithologies, but only the ranges covered differ. The higher enrichments recorded in Hole 923A advocate for a preferential crystallization regime (r between 0.5 and 0.85) except for the Ol-rich sample that follows a trend with a r value of 0.95 (Figure 8c). The (similar) highest fractionation recorded at lower REE contents in Hole U1309D samples advocates for a stronger assimilation regime in this system during the formation of Pl (r value between 0.75 and 0.92, Figure 8d). A little-discussed parameter of the AFC model is F, which is the ratio between the magma mass at a given step and the initial magma mass prior to reaction. The minimum F value required to reproduce Hole U1309D Pl data is slightly lower than that for Hole 923A Pl. This suggests that the amount of melt consumed by melt-mush reactions during the main step of development of the magmatic system (Pl being the main forming mineral in cumulates) is lower at AM (Hole U1309D). These "partial" reactions could result from a more regular or sustained replacement of percolating liquids reacting with the mush minerals.

5.2.5. Clinopyroxene Evolution

Cpx is the last cumulate-forming mineral to crystallize as evidenced by the widespread interstitial textures found in the samples. Large Cpx oikocrysts enclose resorbed Ol and/or Pl chadacrysts, and interstitial Cpx are often in contact with Ol and Pl grains with irregular grain boundaries. This suggests the resorption of Ol and Pl prior to or

during the formation of Cpx. There are no clear resorption textures of Cpx, except potentially for the Cpx intergrowths in the more evolved mineral assemblages. Available thermodynamic models however predict Cpx resorption when present in an Ol gabbro mush assemblage, and crystallization of both Ol and Pl with Cpx during melt-mush reactions (Boulanger & France, 2023). There are no systematic differences in the Cpx textures recorded in Holes U1309D and 923A. Locally more interstitial and less poikilitic Cpx are found in Hole 923A samples, which may suggest smaller volumes of melt during the reactions involved in Cpx formation. Like Pl, the same reaction equation is used for both Holes U1309D and 923A for the evolution of Cpx by AFC:

$$\text{Hole 923A and Hole U1309D, AFC4: } Ol_{25} + Pl_{50} + Cpx_{25} + \text{melt1} \rightarrow Ol_{25} + Pl_{25} + Cpx_{50} + \text{melt2}$$

The significant amount of Ol and Pl in the crystallization assemblage is consistent with the evolution of the REE compositions towards higher fractionation, which could not be reached by Cpx-only crystallization. On the other hand, Cpx assimilation helps reach the enrichment in REE observed in some Cpx. In both sections, the r values implemented in the Cpx modeling are lower and more in favor of a crystallization regime compared to the Ol- and Pl-forming ones (with $r < 0.7$, except in the Ol-rich samples where more assimilation is required, Figures 8e and 8f). This suggests that Cpx appears preferentially past the main assimilation stage, which is consistent with previous AFC and thermodynamic models (Boulanger & France, 2023; Gleeson et al., 2023; Lissenberg & Dick, 2008). The main difference between the two sequences is the wide range of enrichments in REEs recorded in Hole 923A that spread towards high REE contents (Figure 8e). In contrast, Hole U1309D presents Cpx with more restricted composition ranges, showing similar fractionation but lower enrichments in La_N. Taken individually, most Hole U1309D samples present an evolution towards higher fractionation at almost constant enrichments. Associated r values span the same range for both sections (between 0.4 and 0.9). However, in detail, most data from Hole 923A can be reproduced by the model at $r < 0.6$ translating preferential crystallization regime, while higher r ratio between 0.7 and 0.8 are still required to reproduce most U1309D Cpx.

5.3. Implications for Magmatic Accretion at KM and AM

Local evidence for melt-mush reactions was already discussed in both sections, with mantle-melt interactions and the formation of Ol-rich troctolites in Hole U1309D (Drouin et al., 2009, 2010; Ferrando et al., 2018, 2020), especially at the base of the studied section between 1,100 and 1,300 mbsf, and with reactive porous melt transport within the mush in Hole 923A (Coogan et al., 2000; Figure 1). Additional evidence of melt-mush reactions was found in dredged samples and MORBs from the KM area (Leuthold et al., 2018; Lissenberg & Dick, 2008), but the extent of those reactions within both magmatic systems was not established. This study reveals the widespread and strong control of melt-mush reactions on the gabbroic sequences at KM and AM, based on both textures and mineral compositions.

We identified the assimilation of primitive material into both KM and AM gabbroic sequences at various crustal levels. Evidence for assimilation is found either in the textural remnants of the assimilated Ol-rich matrix of the Ol-rich samples or with the primitive reactive melt compositions recorded in some poikilitic or interstitial Cpx. This primitive component could be of mantle origin, especially at AM where mantle assimilation is suspected to result in the formation of Ol-rich troctolites (Ferrando et al., 2018) that share striking compositional similarities with the Ol-rich sample 305-U1309D-228R-4W, 43–46 cm. This hypothesis is also consistent with the general formation dynamics at AM by multiple magma injections into the (mantle) lithosphere (Godard et al., 2009). Mantle slivers could be trapped within the intrusive magmatic sequence, especially at the core complex margins, and assimilated to various extents into the gabbros (sensu lato). However, the evidence provided here is not sufficient to establish the mantle origin of some of the assimilated components in both sections. The very local nature of the primitive signatures recorded by Cpx tells us about the equally local nature of reactive percolation. Indeed, compositional shifts towards the more primitive (Ol-rich) end-member occur at the scale of a few tens of centimeters, confirming the already suspected channelized character of porous melt migration (Coogan et al., 2000; Gleeson et al., 2023).

The majority of the samples, however, record typical melt-mush reactions described in slow-spread crust related to cumulate assimilation. The gabbro textures are heterogeneous in both sections and show no systematics except for the widespread textures of resorption and syn/post resorption crystallization found at different degrees in all samples. The mineral compositions also help appreciate the scale of the impact of melt-mush reaction on differentiation. The systematic shifts in the mineral major elements compared to fractional crystallization trends, and the

REE signatures showing a decoupling with major elements and REE fractionation in almost all of the minerals (especially Pl and Cpx) illustrate the global impact of melt-mush reactions during differentiation. As mentioned earlier, the stronger the fractionation, the stronger the assimilation is likely to occur during the reactions, which would imply overall that a reaction regime involving stronger assimilation was at play during the evolution of AM.

AFC modeling was conducted to help detail these tendencies qualitatively, considering the limitations imposed by the model itself and the scale at which melt-mush reactions are considered. We do not attempt to construct a continuous sequence of reactions between Ol, Pl and Cpx. As mentioned above, the aim of the modeling is to estimate the best conditions of average reactions that impacted the Ol, the Pl, and the Cpx records individually. The potential chemical inheritance of the reactive melt from previous melt-mush reaction steps is also not considered in this strategy. The anticipated effect of such chemical inheritance on sequential AFC models would be a shift in the location of the model starting point (stars in Figure 8). However, this inheritance is difficult to determine at the scale of crustal sequences, considering the scale of the reactions heterogeneity, and with the geochemical tools considered here. The discussion on primitive material assimilation shows the variability in melt composition of the mush system at a scale of a few tens of centimeters. The acquisition of strong chemical heterogeneity potentially increases also with the number of melt-mush reaction steps recorded by the reactive melt. Hence, Cpx being the last mineral to crystallize in the sections, its composition is likely the most difficult to interpret depending on the scale at which the signatures are considered.

Despite the limitations described above, the mineral-by-mineral reactions can be used to discuss the overall dynamics of the systems. The reactions follow the general equation form described in the literature ($Ol \pm Pl \pm Cpx + melt1 \rightarrow Pl \pm Cpx \pm Ol + melt2$). The modes of the mineral assemblages involved in the reactions (Figure 9c) are not quantified and do not reflect any energy constraints. However, the model is still sensitive enough to this parameter to ensure the identification of any significant discrepancies between the modeled evolution trend and the gabbro signatures (Boulanger & France, 2023). A more evolved mineral assemblage crystallizes at AM (AFC1) compared to KM (AFC2) during the earliest stages of magmatic evolution that mainly impact Ol in both sections (Figure 9). Results also show that both assimilated and crystallized assemblages are more primitive in the Ol-based equations (higher proportions of Ol and Pl), and change towards more evolved ones for the Pl-based and Cpx-based equations (higher proportions of Pl and Cpx), resulting in a typical fractionation sequence. In addition to the mineral assemblages, the r ratios indicate greater assimilation during the earliest stage of evolution of the mush (Ol-based equation) and greater crystallization during the latest formation of Cpx. These results are in line with available thermodynamic models (Boulanger & France, 2023), and also with the experimental constraints of Yang et al. (2019).

Comparing the two sections of KM and AM, we find more assimilation evidence during the first steps of formation of both magmatic sequences, probably within a hot and melt-rich environment, which could be consistent with a main melt recharge event. This hypothesis is supported by available thermodynamically constrained models, which show a preferential assimilation regime of melt-dominated melt-mush reactions (Boulanger & France, 2023). In addition, the reactions at AM seem to require slightly more assimilation compared to those at KM, consistent with the r ratios observed in both Pl-based and Cpx-based models. Following the same reasoning, this could result from variations in the melt fraction during melt-mush reactions at the two locations, either by higher melt fractions present within the mush, or by more intense percolation and melt replacement during reactive porous flow. Higher melt supply and/or during longer periods of time at AM would lead to slightly more assimilation and/or a delay in the system closure (Figure 9a). On the other hand, lower melt supply or during shorter amounts of time would result in relatively faster system closure at KM by preferential crystallization during melt-mush reactions, which is consistent with the higher enrichments in incompatible trace elements recorded in Hole 923A minerals.

The type of processes controlling melt differentiation at slow-spreading ridges is the same at the two locations, with strong involvement of melt-mush reactions. The reaction regime, however, is variable, which is consistent with the general accretion dynamics at slow-spreading ridges. Melt supply below the ridge axis is likely intermittent and heterogeneous, both in time and along-axis (e.g., Carbotte et al., 2016; Chen et al., 2023; Cordier et al., 2010, and references therein). The magmatic sections, built by multiple injections of these melts (Godard et al., 2009), have the potential to record such fluctuations. It has been previously suggested by Casey (1997), who inferred from the study of abyssal peridotites, plutonic rocks, and MORBs from the MARK area that "the oceanic crustal architecture may be largely governed by magma supply rate and may lead to a variety and spectrum of

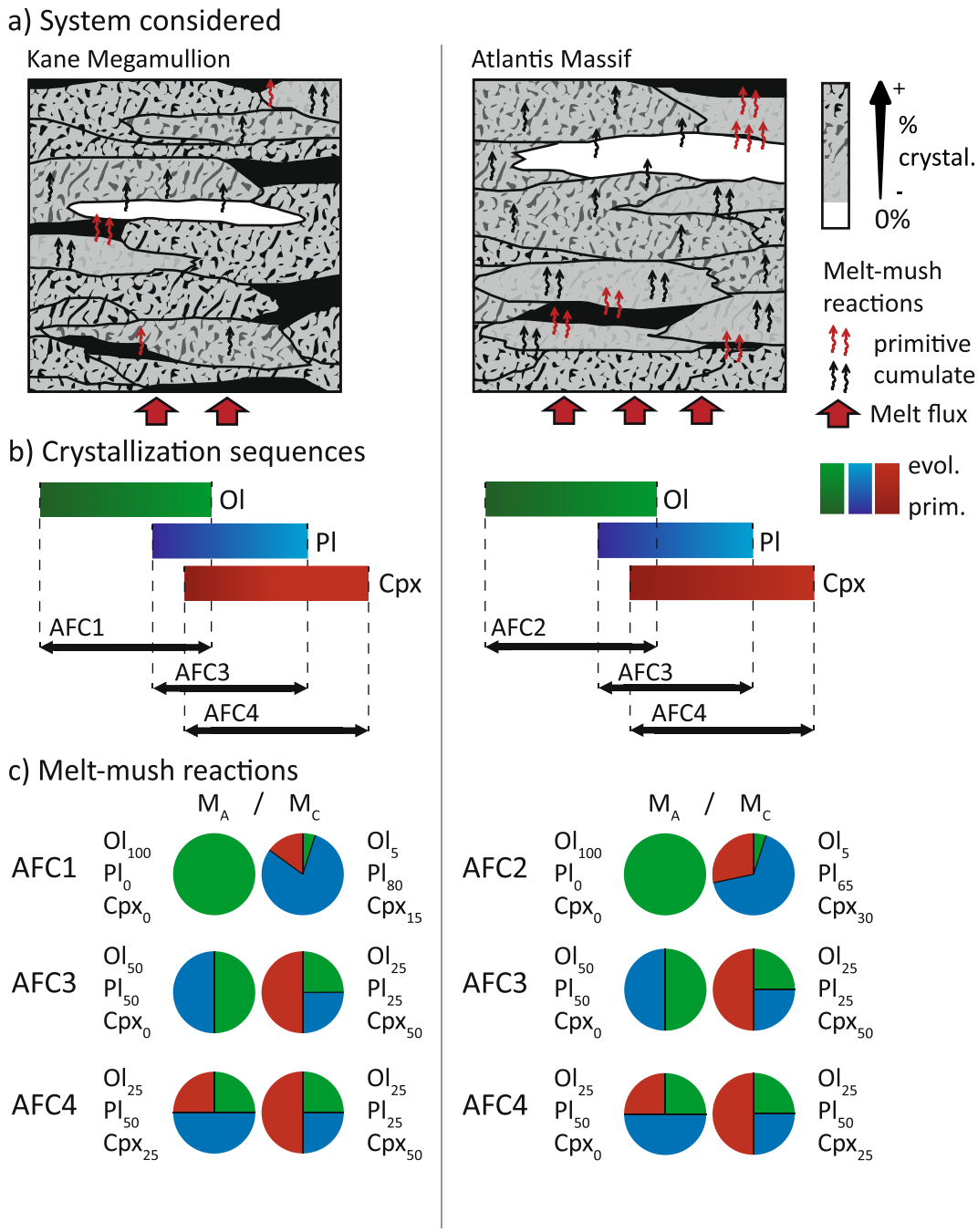

Figure 9. (a) Interpretative model for the formation of the magmatic system at Kane Megamullion (left panels) and Atlantis Massif OCCs (right panels). (c) Modes of the assimilated and crystallized mineral assemblages during the MMR identified in each system (right panels), and described by (b) models AFC1 and AFC2 for Ol, AFC3 for Pl and AFC4 for Cpx.

crustal and upper mantle types." We suggest that melt-mush reaction characteristics can be a marker of variable magma supply rates in both the textures and the geochemical signatures of the cumulates. We also infer here that a large part of the magmatic sequence heterogeneities observed at slow- and ultra-slow-spreading ridges results from melt-mush reactions. The main issue is a scaling problem to reconstruct large-scale processes relying on µm- to cm-scale evidence. Another aspect concerns the extraction of reactive melts from the mush and their potential contribution to MORB compositions. The likeliest moment for melt extraction is when melt fractions and porosity are the highest within the mush, hence during the earliest evolution stage of the reservoirs when more assimilation occurs based on our observations and previous studies (Drouin et al., 2009, 2010; Ferrando et al., 2018, 2020).

The numerical investigation of Hu et al. (2022) on the effect of heating/cooling, compaction, and reactive flow on a simplified diopside-anorthite system shows the complex - sometimes counterintuitive - impact of reactive flow on such a simplified system. It seems to support, however, the effect of reactive flow in enhancing melt fractions of the binary system at "early times." However, reactive flow generally opposes the effect of compaction on the melt fraction and chemical composition of a given mush volume by thermal and/or chemical melting (Hu et al., 2022). The latter process of "chemical melting" is largely overlooked in the thermodynamic modeling of melt-mush reactions, as in Boulanger and France (2023), where only partial melting by temperature increase of the assimilated component is considered for the assimilation stage of melt-mush reaction modeling. A better quantification of melt-mush reactions and porosity evolution associated with kinetics consideration is critical to quantifying the dynamics of magmatic accretion at slow-spreading ridges.

6. Conclusion

The study of the sample textures, and major and trace element compositions of Ol, Pl and Cpx demonstrates the widespread occurrence of melt-mush reactions at both Kane Megamullion and Atlantis Massif. The high-Cr high-Mg# Cpx of some gabbros (sensu lato), and the strong textural resemblance of the latter with Ol-rich troctolites (Drouin et al., 2009, 2010; Ferrando et al., 2018) suggests the assimilation of primitive lithologies (of potential upper mantle origin) within the main gabbro sequences. The latter reactions can be distinguished based on their trace element signatures from typical melt-mush reactions previously described in other slow-spread magmatic systems. Together, these two types of melt-mush reactions significantly contribute to the magmatic evolution of the studied sections. Modeling of the reactions recorded in REE signatures of the three main cumulate-forming minerals (i.e., Ol, Pl, and Cpx) thanks to the AFC model of DePaolo (1981) provides additional insights into the reaction characteristics. The mineral assemblages considered in the assimilated and crystallized components of the reactions are overall similar in the two sections. However, the range of assimilation over crystallization ratios (r) required to reproduce the full data spread varies between Kane Megamullion and Atlantis Massif. Following the reasoning that assimilation is favored in warmer melt-rich environments, differences in the r ratios could result from variations in the melt fraction during melt-mush reactions. This can be achieved either by higher melt fractions present within the mush or by more intense percolation and melt replacement during reactive porous flow. We infer, relying on the latter reasoning, on available thermodynamic modeling, and on previous studies (e.g., Cannat et al., 2019; Casey, 1997; Chen et al., 2023), that the regime of the reactions is most likely controlled by the melt flux during the formation of the two sections. Higher melt flux would lead to higher temperatures of the systems and melt-dominated reactions that would overall favor assimilation and delay system closure by crystallization. Overall, differences in the structure of the magmatic systems and the compositions found in crustal sections recovered at slow-spreading ridges could result from variations in the local melt flux that govern magmatic crustal accretion.

Data Availability Statement

The results of this work are included in the text's main figures, in Figures S1–S7, and in Tables S1, S2 and S5 of the article Supporting Information S1. All major and trace element data used in this study are available online through the OPGC Data Repository via Boulanger et al. (2024).

Acknowledgments

This study was funded through IODP-France to MB, and the bureau IODP-France is heartily thanked for their support. This research used samples and data provided by the Ocean Drilling Program (ODP) and Integrated Ocean Drilling Program (IODP). The assistance of the staff at the Bremen Core Repository is gratefully acknowledged. The authors thank C. Nevado and D. Delmas for careful thin section preparation. The assistance of F. Barou for EBSD, O. Mauguin for EMPA, and O. Bruguier for LA-ICP-MS analyses are thankfully acknowledged. The authors also thank V. Basch and J. Blundy for their thorough and constructive reviews, and P. Asimow for handling this contribution as an editor.

References

Allard, M., Ildefonse, B., Oliot, É., & Barou, F. (2021). Plastic deformation of plagioclase in oceanic gabbro accreted at a slow-spreading ridge (Hole U1473A, Atlantis Bank, Southwest Indian Ridge). *Journal of Geophysical Research: Solid Earth*, *126*(10), e2021JB021964. https://doi.org/10.1029/2021JB021964

Basch, V., Drury, M. R., Plumper, O., Hellebrand, E., Crispini, L., Barou, F., et al. (2021). Intracrystalline melt migration in deformed olivine revealed by trace element compositions and polyphase solid inclusions. *European Journal of Mineralogy*, *33*(4), 463–477. https://doi.org/10.5194/ejm-33-463-2021

Basch, V., Rampone, E., Crispini, L., Ferrando, C., Ildefonse, B., & Godard, M. (2019). Multi-stage reactive formation of troctolites in slow-spreading oceanic lithosphere (Erro-Tobbio, Italy): A combined field and petrochemical study. *Journal of Petrology*, *60*(5), 873–906. https://doi.org/10.1093/petrology/egz019

Basch, V., Sanfilippo, A., Skolotnev, S. G., Ferrando, C., Muccini, F., Palmiotto, C., et al. (2022). Genesis of oceanic oxide gabbros and gabbronorites during reactive melt migration at transform walls (Doldrums Megatransform System; 7–8°N Mid-Atlantic Ridge). *Journal of Petrology*, *63*(9), 1–23. https://doi.org/10.1093/petrology/egac086

Basch, V., Sanfilippo, A., Snow, J. E., Loocke, M., & Zanetti, A. (2024). Accretion of the lower oceanic crust at fast-spreading ridges: Insights from Hess Deep (East Pacific Rise, IODP Expedition 345). *Journal of Petrology*, *65*(6), egae048. https://doi.org/10.1093/petrology/egae048

Bédard, J. H. (2001). Parental magmas of the nain plutonic suite anorthosites and mafic cumulates: A trace element modelling approach. *Contributions to Mineralogy and Petrology*, *141*(6), 747–771. https://doi.org/10.1007/s004100100268

Blackman, D. K., Canales, J. P., & Harding, A. (2009). Geophysical signatures of oceanic core complexes. *Geophysical Journal International*, *178*(2), 593–613. https://doi.org/10.1111/j.1365-246X.2009.04184.x

Blackman, D. K., Ildefonse, B., John, B. E., Ohara, Y., Miller, D. J., Abe, N., et al. (2011). Drilling constraints on lithospheric accretion and evolution at Atlantis Massif, Mid-Atlantic Ridge 30°N. *Journal of Geophysical Research*, *116*(7), B07103. https://doi.org/10.1029/2010JB007931

Blackman, D. K., Ildefonse, B., John, B. E., Ohara, Y., Miller, D. J., & Macleod, C. J. (2006). Site U1309. *Proceedings of the IODP*, *304/305*, 304. https://doi.org/10.2204/iodp.proc.304305.103.2006

Blackman, D. K., Karson, J. A., Kelley, D. S., Cann, J. R., Früh-Green, G. L., Gee, J. S., et al. (2004). Geology of the Atlantis Massif (Mid-Atlantic Ridge, 30°N): Implications for the evolution of an ultramafic oceanic core complex. *Marine Geophysical Research*, *23*(5–6), 443–469. https://doi.org/10.1023/b:mari.0000018232.14085.75

Bloomer, S. H., Meyer, P. S., Dick, H. J. B., Ozawa, K., & Natland, J. H. (1991). Textural and mineralogical variations in gabbroic rocks from Hole 735B. In *Proceedings of the Ocean Drilling Program, 118 Scientific Results*. Ocean Drilling Program. https://doi.org/10.2973/odp.proc.sr.118.136.1991

Bodinier, J. L., Vasseur, G., Vernieres, J., Dupuy, C., & Fabries, J. (1990). Mechanisms of mantle metasomatism: Geochemical evidence from the Lherz Orogenic Peridotite. *Journal of Petrology*, *31*(3), 597–628. https://doi.org/10.1093/petrology/31.3.597

Borghini, G., & Rampone, E. (2007). Postcumulus processes in oceanic-type olivine-rich cumulates: The role of trapped melt crystallization versus melt/rock interaction. *Contributions to Mineralogy and Petrology*, *154*(6), 619–633. https://doi.org/10.1007/s00410-007-0217-5

Boulanger, M., & France, L. (2023). Cumulate formation and melt extraction from mush-dominated magma reservoirs: The melt flush process exemplified at mid-ocean ridges. *Journal of Petrology*, *64*(2), 1–20. https://doi.org/10.1093/petrology/egad005

Boulanger, M., France, L., Deans, J. R. L., Ferrando, C., Lissenberg, C. J., & von der Handt, A. (2020). Magma reservoir formation and evolution at a slow-spreading center (Atlantis Bank, Southwest Indian Ridge). *Frontiers in Earth Science*, *8*, 554598. https://doi.org/10.3389/feart.2020.554598

Boulanger, M., France, L., Ferrando, C., Ildefonse, B., Ghosh, B., Sanfilippo, A., et al. (2021). Magma-mush interactions in the lower oceanic crust: Insights from Atlantis bank layered series (Southwest Indian Ridge). *Journal of Geophysical Research: Solid Earth*, *126*(9), e2021JB022331. https://doi.org/10.1029/2021JB022331

Boulanger, M., Godard, M., Ildefonse, B., & Bakouche, M. (2024). Petrological evidence for prominent melt-mush reactions during slow-spreading oceanic accretion [Dataset]. *OPGC, LMV*. https://doi.org/10.25519/1YG4-AQ12

Buck, W. R., Lavier, L. L., & Poliakov, A. N. B. (2005). Modes of faulting at mid-ocean ridges. *Nature*, *434*(7034), 719–723. https://doi.org/10.1038/nature03358

Canales, J. P., Dunn, R. A., Arai, R., & Sohn, R. A. (2017). Seismic imaging of magma sills beneath an ultramafic-hosted hydrothermal system. *Geology*, *45*(5), 451–454. https://doi.org/10.1130/G38795.1

Canales, J. P., Tucholke, B. E., Xu, M., Collins, J. A., & DuBois, D. L. (2008). Seismic evidence for large-scale compositional heterogeneity of oceanic core complexes. *Geochemistry, Geophysics, Geosystems*, *9*(8), Q08002. https://doi.org/10.1029/2008GC002009

Cann, J. R., Blackman, D. K., Smith, D. K., McAllister, E., Janssen, B., Mello, S., et al. (1997). Corrugated slip surfaces formed at ridge-transform intersections on the Mid-Atlantic Ridge. *Nature*, *385*(6614), 329–332. https://doi.org/10.1038/385329a0

Cannat, M., Chatin, F., Whitechurch, H., & Ceuleneer, G. (1997). Gabbroic rocks trapped in the upper mantle at the Mid-Atlantic Ridge. *Proceedings of the Ocean Drilling Program: Scientific Results*, *153*, 243–264. https://doi.org/10.2973/odp.proc.sr.153.013.1997

Cannat, M., Karson, J. A., & Miller, D. J. (1995). Site 923. In *Proceedings of the Ocean Drilling Program, Initial Reports* (Vol. 153). Ocean Drilling Program. https://doi.org/10.2973/odp.proc.ir.153.105.1995

Cannat, M., Karson, J. A., Miller, D. J., & Party, S. S. (1995). ODP Leg 153 MARK Initial Report. In *Proceedings ODP Initial Reports* (Vol. 153).

Cannat, M., Sauter, D., Lavier, L., Bickert, M., Momoh, E., & Leroy, S. (2019). On spreading modes and magma supply at slow and ultraslow mid-ocean ridges. *Earth and Planetary Science Letters*, *519*, 223–233. https://doi.org/10.1016/j.epsl.2019.05.012

Carbotte, S. M., Smith, D. K., Cannat, M., & Klein, E. M. (2016). Tectonic and magmatic segmentation of the global ocean ridge system: A synthesis of observations. *Geological Society, London, Special Publications*, *420*(1), 249–295. https://doi.org/10.1144/sp420.5

Casey, J. (1997). Comparison of major- and trace element geochemistry of abyssal peridotites and mafic plutonic rocks with basalts from the MARK region of the Mid-Atlantic Ridge. *Proceedings of the Ocean Drilling Program, Scientific Results*, *153*(1987), 181–241. https://doi.org/10.2973/odp.proc.sr.153.012.1997

Chen, J., Olive, J., & Cannat, M. (2023). Beyond spreading rate: Controls on the thermal regime of mid-ocean ridges. *Proceedings of the National Academy of Sciences*, *120*(45), 2017. https://doi.org/10.1073/pnas.2306466120

Coogan, L. A., Saunders, A. D., Kempton, P. D., & Norry, M. J. (2000). Evidence from oceanic gabbros for porous melt migration within a crystal mush beneath the Mid-Atlantic Ridge. *Geochemistry, Geophysics, Geosystems*, *1*(9). https://doi.org/10.1029/2000GC000072

Coogan, L. A., Wilson, R. N., Gillis, K. M., & MacLeod, C. J. (2001). Near-solidus evolution of oceanic gabbros: Insights from amphibole geochemistry. *Geochimica et Cosmochimica Acta*, *65*(23), 4339–4357. https://doi.org/10.1016/S0016-7037(01)00714-1

Cordier, C., Benoit, M., Hémond, C., Dyment, J., Gall, B. L., Briais, A., & Kitazawa, M. (2010). Time scales of melt extraction revealed by distribution of lava composition across a ridge axis. *Geochemistry, Geophysics, Geosystems*, *11*(7), Q0AC06. https://doi.org/10.1029/2010GC003074

Danyushevsky, L. V., Perfit, M. R., Eggins, S. M., & Falloon, T. J. (2003). Crustal origin for coupled "ultra-depleted" and "plagioclase" signatures in MORB olivine-hosted melt inclusions: Evidence from the Siqueiros Transform Fault, East Pacific Rise. *Contributions to Mineralogy and Petrology*, *144*(5), 619–637. https://doi.org/10.1007/s00410-002-0420-3

DePaolo, D. J. (1981). Trace element and isotopic effects of combined wallrock assimilation and fractional crystallization. *Earth and Planetary Science Letters*, *53*(2), 189–202. https://doi.org/10.1016/0012-821X(81)90153-9

Dick, H. J. B., Kvassnes, A. J. S., Robinson, P. T., MacLeod, C. J., & Kinoshita, H. (2019). The Atlantis Bank Gabbro Massif, Southwest Indian Ridge. *Progress in Earth and Planetary Science*, *6*(1), 64. https://doi.org/10.1186/s40645-019-0307-9

Dick, H. J. B., MacLeod, C. J., Blum, P., Abe, N., Blackman, D. K., Bowles, J. A., et al. (2019). Dynamic accretion beneath a slow-spreading ridge segment: IODP Hole 1473A and the Atlantis Bank oceanic core complex. *Journal of Geophysical Research: Solid Earth*, *124*(12), 12631–12659. https://doi.org/10.1029/2018JB016858

Dick, H. J. B., Natland, J. H., Miller, D. J., & Al, E. (1999). Site 735. In *Proceedings of the Ocean Drilling Program* (Vol. 176).

Dick, H. J. B., Tivey, M. A., & Tucholke, B. E. (2008). Plutonic foundation of a slow-spreading ridge segment: Oceanic core complex at Kane Megamullion, 23°30′N, 45°20′W. *Geochemistry, Geophysics, Geosystems*, *9*(5), Q05014. https://doi.org/10.1029/2007GC001645

Drouin, M., Godard, M., Ildefonse, B., Bruguier, O., & Garrido, C. J. (2009). Geochemical and petrographic evidence for magmatic impregnation in the oceanic lithosphere at Atlantis Massif, Mid-Atlantic Ridge (IODP Hole U1309D, 30°N). *Chemical Geology*, *264*(1–4), 71–88. https://doi.org/10.1016/j.chemgeo.2009.02.013

Drouin, M., Ildefonse, B., & Godard, M. (2010). A microstructural imprint of melt impregnation in slow spreading lithosphere: Olivine-rich troctolites from the Atlantis Massif, Mid-Atlantic Ridge, 30°N, IODP Hole U1309D. *Geochemistry, Geophysics, Geosystems*, *11*(6), Q06003. https://doi.org/10.1029/2009GC002995

Escartín, J., Smith, D. K., Cann, J., Schouten, H., Langmuir, C. H., & Escrig, S. (2008). Central role of detachment faults in accretion of slow-spreading oceanic lithosphere. *Nature*, *455*(7214), 790–794. https://doi.org/10.1038/nature07333

Ferrando, C., Basch, V., Ildefonse, B., Deans, J., Sanfilippo, A., Barou, F., & France, L. (2021). Role of compaction in melt extraction and accumulation at a slow spreading center: Microstructures of olivine gabbros from the Atlantis Bank (IODP Hole U1473A, SWIR). *Tectonophysics*, *815*, 229001. https://doi.org/10.1016/j.tecto.2021.229001

Ferrando, C., France, L., Basch, V., Sanfilippo, A., Tribuzio, R., & Boulanger, M. (2021). Grain size variations record segregation of residual melts in slow-spreading oceanic crust (Atlantis Bank, 57°E Southwest Indian Ridge). *Journal of Geophysical Research: Solid Earth*, *126*(4), 1–27. https://doi.org/10.1029/2020JB020997

Ferrando, C., Godard, M., Ildefonse, B., & Rampone, E. (2018). Melt transport and mantle assimilation at Atlantis Massif (IODP Site U1309): Constraints from geochemical modeling. *Lithos*, *323*, 24–43. https://doi.org/10.1016/j.lithos.2018.01.012

Ferrando, C., Lynn, K. J., Basch, V., Ildefonse, B., & Godard, M. (2020). Retrieving timescales of oceanic crustal evolution at Oceanic Core Complexes: Insights from diffusion modelling of geochemical profiles in olivine. *Lithos*, *376–377*, 105727. https://doi.org/10.1016/j.lithos.2020.105727

Ferrando, C., Tribuzio, R., Lissenberg, C. J., France, L., MacLeod, C. J., Basch, V., et al. (2022). Brown amphibole as tracer of tectono-magmatic evolution of the Atlantis Bank oceanic core complex (IODP Hole U1473A). *Journal of Petrology*, *63*(9), 1–27. https://doi.org/10.1093/petrology/egac089

Fujibayashi, N., Kagami, H., & Oishi, Y. (1997). Data report: Mineralogy and Sr- and Nd-isotopic composition of gabbroic oceanic crust recovered from Holes 923A and 921E in the MARK area. In *Proceedings of the Ocean Drilling Program*, *Scientific Results* (Vol. 153). https://doi.org/10.2973/odp.proc.sr.153.028.1997

Gao, Y., Hoefs, J., Hellebrand, E., von der Handt, A., & Snow, J. E. (2007). Trace element zoning in pyroxenes from ODP Hole 735B gabbros: Diffusive exchange or synkinematic crystal fractionation? *Contributions to Mineralogy and Petrology*, *153*(4), 429–442. https://doi.org/10.1007/s00410-006-0158-4

Gardner, R. L., Daczko, N. R., & Piazolo, S. (2023). The critical role of deformation-assisted melt migration in the formation of oceanic core complexes. *Australian Journal of Earth Sciences*, *71*(1), 1–21. https://doi.org/10.1080/08120099.2023.2259451

Gardner, R. L., Piazolo, S., Daczko, N. R., & Trimby, P. (2020). Microstructures reveal multistage melt present strain localisation in mid-ocean gabbros. *Lithos*, *366–367*, 105572. https://doi.org/10.1016/j.lithos.2020.105572

Gleeson, M. L. M., Lissenberg, C. J., & Antoshechkina, P. M. (2023). Porosity evolution of mafic crystal mush during reactive flow. *Nature Communications*, *14*(1), 3088. https://doi.org/10.1038/s41467-023-38136-x

Godard, M., Awaji, S., Hansen, H., Hellebrand, E., Brunelli, D., Johnson, K., et al. (2009). Geochemistry of a long in-situ section of intrusive slow-spread oceanic lithosphere: Results from IODP Site U1309 (Atlantis Massif, 30°N Mid-Atlantic-Ridge). *Earth and Planetary Science Letters*, *279*(1–2), 110–122. https://doi.org/10.1016/j.epsl.2008.12.034

Godard, M., Bodinier, J. L., & Vasseur, G. (1995). Effects of mineralogical reactions on trace element redistributions in mantle rocks during percolation processes: A chromatographic approach. *Earth and Planetary Science Letters*, *133*(3–4), 449–461. https://doi.org/10.1016/0012-821X(95)00104-K

Grimes, C. B., John, B. E., Cheadle, M. J., & Wooden, J. L. (2008). Protracted construction of gabbroic crust at a slow spreading ridge: Constraints from $^{206}Pb/^{238}U$ zircon ages from Atlantis Massif and IODP Hole U1309D (30°N, MAR). *Geochemistry, Geophysics, Geosystems*, *9*(8), Q08012. https://doi.org/10.1029/2008GC002063

Holness, M. B., Vukmanovic, Z., & Mariani, E. (2017). Assessing the role of compaction in the formation of adcumulates: A microstructural perspective. *Journal of Petrology*, *58*(4), 643–674. https://doi.org/10.1093/petrology/egx037

Hu, H., Jackson, M. D., & Blundy, J. (2022). Melting, compaction and reactive flow: Controls on melt fraction and composition change in crustal mush reservoirs. *Journal of Petrology*, *63*(11), 1–28. https://doi.org/10.1093/petrology/egac097

Kelemen, P. B., Dick, H. J. B., & Quick, J. E. (1992). Formation of harzburgite by pervasive melt/rock reaction in the upper mantle. *Nature*, *358*(6388), 635–641. https://doi.org/10.1038/358635a0

Koepke, J., Feig, S., & Snow, J. (2005). Late stage magmatic evolution of oceanic gabbros as a result of hydrous partial melting: Evidence from the Ocean Drilling Program (ODP) Leg 153 drilling at the Mid-Atlantic Ridge. *Geochemistry, Geophysics, Geosystems*, *6*(2), Q02001. https://doi.org/10.1029/2004GC000805

Kvassnes, A. J. S., Strand, A. H., Moen-Eikeland, H., & Pedersen, R. B. (2004). The Lyngen Gabbro: The lower crust of an Ordovician Incipient Arc. *Contributions to Mineralogy and Petrology*, *148*(3), 358–379. https://doi.org/10.1007/s00410-004-0609-8

Laubier, M., Gale, A., & Langmuir, C. H. (2012). Melting and crustal processes at the FAMOUS segment (Mid-Atlantic Ridge): New insights from olivine-hosted melt inclusions from multiple samples. *Journal of Petrology*, *53*(4), 665–698. https://doi.org/10.1093/petrology/egr075

Leuthold, J., Lissenberg, C. J., O'Driscoll, B., Karakas, O., Falloon, T., Klimentyeva, D. N., & Ulmer, P. (2018). Partial melting of lower oceanic crust gabbro: Constraints from poikilitic clinopyroxene primocrysts. *Frontiers in Earth Science*, *6*, 15. https://doi.org/10.3389/feart.2018.00015

Lissenberg, C. J., & Dick, H. J. B. (2008). Melt-rock reaction in the lower oceanic crust and its implications for the genesis of mid-ocean ridge basalt. *Earth and Planetary Science Letters*, *271*(1–4), 311–325. https://doi.org/10.1016/j.epsl.2008.04.023

Lissenberg, C. J., & MacLeod, C. J. (2016). A reactive porous flow control on mid-ocean ridge magmatic evolution. *Journal of Petrology*, *57*(11–12), 2195–2220. https://doi.org/10.1093/petrology/egw074

Lissenberg, C. J., MacLeod, C. J., & Bennett, E. N. (2019). Consequences of a crystal mush-dominated magma plumbing system: A mid-ocean ridge perspective. *Philosophical Transactions of the Royal Society A: Mathematical, Physical & Engineering Sciences*, *377*(2139), 20180014. https://doi.org/10.1098/rsta.2018.0014

Lissenberg, C. J., MacLeod, C. J., Howard, K. A., & Godard, M. (2013). Pervasive reactive melt migration through fast-spreading lower oceanic crust (Hess Deep, equatorial Pacific Ocean). *Earth and Planetary Science Letters*, *361*, 436–447. https://doi.org/10.1016/j.epsl.2012.11.012

MacLeod, C. J., Dick, H. J. B., Blum, P., Abe, N., Blackman, D. K., Bowles, J. A., et al. (2017). Site U1473. *Proceedings of the Ocean Drilling Program*, *360*. https://doi.org/10.14379/iodp.proc.360.103.2017

Mainprice, D., Bachmann, F., Hielscher, R., & Schaeben, H. (2014). Descriptive tools for the analysis of texture projects with large datasets using MTEX: Strength, symmetry and components. *Geological Society, London, Special Publications*, *409*(1), 251–271. https://doi.org/10.1144/SP409.8

Mainprice, D., & Silver, P. G. (1993). Interpretation of SKS-waves using samples from the subcontinental lithosphere. *Physics of the Earth and Planetary Interiors*, *78*(3–4), 257–280. https://doi.org/10.1016/0031-9201(93)90160-B

Mathez, E. A. (1995). Magmatic metasomatism and formation of the Merensky reef, Bushveld Complex. *Contributions to Mineralogy and Petrology*, *119*(2–3), 277–286. https://doi.org/10.1007/BF00307287

McDonough, W. F., & Sun, S. S. (1995). The composition of the Earth. *Chemical Geology*, *120*(3–4), 223–253. https://doi.org/10.1016/0009-2541(94)00140-4

Miller, D. J., Abratis, M., Christie, D., Drouin, M., Godard, M., Ildefonse, B., et al. (2009). Data report: Microprobe analyses of primary mineral phases from Site U1309, Atlantis Massif, IODP Expedition 304/305. In *Proceedings of the IODP* (Vol. 304/305). Integrated Ocean Drilling Program. https://doi.org/10.2204/iodp.proc.304305.202.2009

Niida, K. (1997). Mineralogy of MARK peridotites: Replacement through magma channeling examined from Hole 920D, MARK area. In *Proceedings of the Ocean Drilling Program*, *Scientific Results* (Vol. 153, pp. 265–275). https://doi.org/10.2973/odp.proc.sr.153.014.1997

Nooner, S. L., Sasagawa, G. S., Blackman, D. K., & Zumberge, M. A. (2003). Structure of oceanic core complexes: Constraints from seafloor gravity measurements made at the Atlantis Massif. *Geophysical Research Letters*, *30*(8), 8–11. https://doi.org/10.1029/2003GL017126

Paquet, M., Cannat, M., Brunelli, D., Hamelin, C., & Humler, E. (2016). Effect of melt/mantle interactions on MORB chemistry at the easternmost Southwest Indian Ridge (61°–67°E). *Geochemistry, Geophysics, Geosystems*, *17*(11), 4605–4640. https://doi.org/10.1002/2016GC006385

Pearce, N. J. G., Perkins, W. T., Westgate, J. A., Gorton, M. P., Jackson, S. E., Neal, C. R., & Chenery, S. P. (1997). A compilation of new and published major and trace element data for NIST SRM 610 and NIST SRM 612 glass reference materials. *Geostandards Newsletter*, *21*(1), 115–144. https://doi.org/10.1111/j.1751-908X.1997.tb00538.x

Rampone, E., Borghini, G., Godard, M., Ildefonse, B., Crispini, L., & Fumagalli, P. (2016). Melt/rock reaction at oceanic peridotite/gabbro transition as revealed by trace element chemistry of olivine. *Geochimica et Cosmochimica Acta*, *190*, 309–331. https://doi.org/10.1016/j.gca.2016.06.029

Reiners, P. W. (1998). Reactive melt transport in the mantle and geochemical signatures of mantle-derived magmas. *Journal of Petrology*, *39*(5), 1039–1061. https://doi.org/10.1093/petroj/39.5.1039

Ross, K., & Elthon, D. (1997). Cumulus and postcumulus crystallization in the oceanic crust: Major- and trace-element geochemistry of Leg 153 gabbroic rocks. In *Proceedings of the Ocean Drilling Program*, *Scientific Results* (Vol. 153, pp. 333–353). Ocean Drilling Program. https://doi.org/10.2973/odp.proc.sr.153.023.1997

Ryan, W. B. F., Carbotte, S. M., Coplan, J. O., Hara, S. O., Melkonian, A., Arko, R., et al. (2009). Global multi-resolution topography synthesis. *Geochemistry, Geophysics, Geosystems*, *10*(3), Q03014. https://doi.org/10.1029/2008GC002332

Sanfilippo, A., Macleod, C. J., Tribuzio, R., Lissenberg, C. J., & Zanetti, A. (2020). Early-stage melt-rock reaction in a cooling crystal mush beneath a (IODP Hole U1473A, Atlantis Bank, Southwest Indian Ridge). *Frontiers in Earth Science*, *8*, 1–21. https://doi.org/10.3389/feart.2020.579138

Sanfilippo, A., & Tribuzio, R. (2013). Building of the deepest crust at a fossil slow-spreading centre (Pineto gabbroic sequence, Alpine Jurassic ophiolites). *Contributions to Mineralogy and Petrology*, *165*(4), 705–721. https://doi.org/10.1007/s00410-012-0831-8

Sanfilippo, A., Tribuzio, R., & Tiepolo, M. (2014). Mantle-crust interactions in the oceanic lithosphere: Constraints from minor and trace elements in olivine. *Geochimica et Cosmochimica Acta*, *141*, 423–439. https://doi.org/10.1016/j.gca.2014.06.012

Sanfilippo, A., Tribuzio, R., Tiepolo, M., & Berno, D. (2015). Reactive flow as dominant evolution process in the lowermost oceanic crust: Evidence from olivine of the Pineto ophiolite (Corsica). *Contributions to Mineralogy and Petrology*, *170*(4), 1–12. https://doi.org/10.1007/s00410-015-1194-8

Satsukawa, T., Ildefonse, B., Mainprice, D., Morales, L. F. G., Michibayashi, K., & Barou, F. (2013). A database of plagioclase crystal preferred orientations (CPO) and microstructures-implications for CPO origin, strength, symmetry and seismic anisotropy in gabbroic rocks. *Solid Earth*, *4*(2), 511–542. https://doi.org/10.5194/se-4-511-2013

Schneider, C. A., Rasband, W. S., & Eliceiri, K. W. (2012). NIH Image to ImageJ: 25 years of Image Analysis. *Nature Methods*, *9*(7), 671–675. https://doi.org/10.1038/nmeth.2089

Shimizu, K., Saal, A. E., Hauri, E. H., Perfit, M. R., & Hékinian, R. (2019). Evaluating the roles of melt-rock interaction and partial degassing on the CO_2/Ba ratios of MORB: Implications for the CO2 budget in the Earth's depleted upper mantle. *Geochimica et Cosmochimica Acta*, *260*, 29–48. https://doi.org/10.1016/j.gca.2019.06.013

Smith, D., Escartín, J., Schouten, H., & Cann, J. (2012). Active long-lived faults emerging along slow-spreading mid-ocean ridges. *Oceanography*, *25*(1), 94–99. https://doi.org/10.5670/oceanog.2012.07

Sparks, R. S. J., Annen, C., Blundy, J. D., Cashman, K. V., Rust, A. C., & Jackson, M. D. (2019). Formation and dynamics of magma reservoirs. *Philosophical Transactions of the Royal Society A*, *377*(2139), 20180019. https://doi.org/10.1098/rsta.2018.0019

Suhr, G., Hellebrand, E., Johnson, K., & Brunelli, D. (2008). Stacked gabbro units and intervening mantle: A detailed look at a section of IODP Leg 305, hole U1309D. *Geochemistry, Geophysics, Geosystems*, *9*(10), Q10007. https://doi.org/10.1029/2008GC002012

Tamura, A., Arai, S., Ishimaru, S., & Andal, E. S. (2008). Petrology and geochemistry of peridotites from IODP Site U1309 at Atlantis Massif, MAR 30°N: Micro- and macro-scale melt penetrations into peridotites. *Contributions to Mineralogy and Petrology*, *155*(4), 491–509. https://doi.org/10.1007/s00410-007-0254-0

Vernières, J., Godard, M., & Bodinier, J.-L. (1997). A plate model for the simulation of trace element fractionation during partial melting and magma transport in the Earth's upper mantle. *Journal of Geophysical Research*, *102*(B11), 24771–24784. https://doi.org/10.1029/97jb01946

Yang, A. Y., Wang, C., Liang, Y., & Lissenberg, C. J. (2019). Reaction between MORB magma and lower oceanic crust: An experimental study. *Geochemistry, Geophysics, Geosystems*, *20*(9), 4390–4407. https://doi.org/10.1029/2019GC008368

Zhang, W.-Q., Dick, H. J. B., Liu, C.-Z., Lin, Y.-Z., & Angeloni, L. M. (2021). MORB melt transport through Atlantis Bank oceanic batholith (SW Indian Ridge). *Journal of Petrology*, *62*(6), egab034. https://doi.org/10.1093/petrology/egab034

Zhang, W.-Q., & Liu, C.-Z. (2023). Crust-scale reactive porous flow revealed by the brown amphibole in the IODP hole U1473A gabbros, Southwest Indian Ridge. *Lithos*, *450–451*, 107209. https://doi.org/10.1016/j.lithos.2023.107209

Zhang, W.-Q., Liu, C.-Z., & Dick, H. J. B. (2020). Evidence for multi-stage melt transport in the lower ocean crust: The Atlantis Bank Gabbroic Massif (IODP Hole U1473A, SW Indian Ridge). *Journal of Petrology*, *61*(9), egaa082. https://doi.org/10.1093/petrology/egaa082

References From the Supporting Information

Cheadle, M. J., & Gee, J. S. (2017). Quantitative textural insights into the formation of gabbro in mafic intrusions. *Elements*, *13*(6), 409–414. https://doi.org/10.2138/gselements.13.6.409